Coastal REsearch And Transportation Education
Tier 1 University Transportation Center
U.S. Department of Transportation

Composite Mangroves for Reducing Soil Erosion near Transportation Infrastructure
August 31, 2025

(1) Ayush Kumar, Graduate Student, Zachry Department of Civil and Environmental Engineering, Texas A&M University, College Station, TX 77843-3136; Email: aayush010@tamu.edu
(2) Anand J. Puppala, Ph.D., P.E., BC.GE, F-ICE, Dist. M.ASCE, A.P. & Florence Wiley Chair Professor, Zachry Department of Civil and Environmental Engineering, Texas A&M University, College Station, TX 77843-3136; Email: anandp@tamu.edu

Final Research Report
Prepared for:
Coastal REsearch And Transportation Education

CREATE

Technical Report Documentation Form

1. Report No.	2. Government Accession No.	3. Recipient's Catalog No.
2301-5	01895248	n/a

4. Title and Subtitle

Composite Mangroves for Reducing Soil Erosion near Transportation Infrastructure

5. Report Date

8/31/2025

6. Performing Organization Code

n/a

7. Author(s) : Ayush Kumar, grad student, Zachary Department of Civil and Enviromental Engineering, Texas A&M University, College Station, TX 77843-3136, Anand J Puppala, PhD.,P.E. BC.GE, F-ICE, Dist MASCE, a.p. & Florence Wiley Chair Prof. Zachry Dept. Civil and Environmental Eng. Texas A&M U College Stateion, TX 77843 Email: anandp@tamu.edu

8. Performing Organization Report No.

n/a

9. Performing Organization Name and Address

Zachry Department of Civil and Environmental Engineering, Texas A&M University, College Station, TX 77843-3136

10. Work Unit No. (TRAIS)

n/a

12. Sponsoring Agency Name and Address

Office of the Assistant Secretary for Research and Technology
University Transportation Centers Program
Department of Transportation
Washington, DC United States 20590

11. Contract or Grant No.

69A3552348330

13. Type of Report and Period Covered

Final Project Report
9/01/2023-8/31/2025

14. Sponsoring Agency Code

OST-R

15. Supplementary Notes

https://create.engineering.txst.edu/

16. Abstract

The intensification of coastal stressors and rising coastal urbanization necessitate innovative alternatives to conventional hard engineering structures for coastal embankment protection. While mangrove ecosystems demonstrate proven capabilities for attenuating wave energy, their effectiveness in protecting coastal transportation infrastructure remains inadequately understood. This study evaluated nature-inspired artificial mangrove systems for mitigating incoming wave energy and reducing coastal embankment erosion through laboratory-scale experimentation and numerical modeling. A comparative investigation between control and mangrove-protected embankment configurations under identical hydrodynamic loading was performed in a wave flume facility at Texas A&M University, Galveston. Artificial mangroves replicated characteristics of Rhizophora mangle (red mangrove) at a 1:15 geometric scale, incorporating trunk-root systems in staggered arrangements. Progressive wave cycles simulated storm intensification by increasing wave parameters. Free surface elevation was monitored using capacitance-type wave gauges, while laser scanning systems measured the temporal evolution of the embankment profile. Numerical validation was conducted using FLOW-3D® HYDRO with multi-physics modeling including turbulence, sediment transport, and wave-structure interaction components. Results demonstrate that mangrove-protected configurations achieved wave height reductions of 16-45% compared to 8-18% in control scenarios, with maximum energy dissipation reaching 44% under optimal wave-mangrove interaction conditions. Transmission coefficient analysis showed higher energy dissipation performance throughout all experimental cycles. Embankment erosion analysis revealed a 45% reduction in embankment erosion during optimal conditions, when wave crests achieved complete interaction with the submerged root system. However, effectiveness decreased when elevated water levels allowed wave propagation above the effective root zones. Profile evolution analysis revealed distinct morphological responses, with mangrove-protected embankments exhibiting concentrated pivot points and proximal sandbar formation, indicating enhanced energy dissipation and reduced wave reflection compared to unprotected configurations. Numerical modeling reproduced wave transformation characteristics but revealed limitations in capturing complex morphological processes due to the absence of unsaturated soil mechanics parameters in current sediment transport formulations. The findings demonstrate that nature-based artificial mangrove systems effectively enhance coastal embankment resilience through wave energy attenuation, offering a viable solution for protecting transportation infrastructure. The submergence-dependent performance characteristics highlight the critical importance of design optimization for relative positioning between wave energy and vegetation architecture. These results provide essential foundations for developing practical implementation guidelines for artificial mangrove systems in coastal protection applications.

17. Key Words	18. Distribution Statement
Artificial Mangrove Systems, Coastal Protection, Wave Attenuation, Embankment Erosion, Transportation Infrastructure, Nature-Based Solutions	No Restrictions

19. Security Classification (of this report)	20. Security Classification (of this page)	21. No. of Pages	22. Price
Unclassified	Unclassified	49	n/a

ACKNOWLEDGMENT

This study was funded, partially or entirely, by the U.S. Department of Transportation through the Coastal REsearch and Transportation Education University Transportation Center under Grant Award Number 69A3552348330. The work was conducted at Texas A&M University, College Station, and Texas A&M University, Galveston.

DISCLAIMER

The contents of this report reflect the views of the authors, who are responsible for the facts and the accuracy of the information presented herein. This document is disseminated under the sponsorship of the U.S. Department of Transportation's University Transportation Centers Program, in the interest of information exchange. The U.S. Government assumes no liability for the contents or use thereof.

ABSTRACT

The intensification of coastal stressors and rising coastal urbanization necessitate innovative alternatives to conventional hard engineering structures for coastal embankment protection. While mangrove ecosystems demonstrate proven capabilities for attenuating wave energy, their effectiveness in protecting coastal transportation infrastructure remains inadequately understood. This study evaluated nature-inspired artificial mangrove systems for mitigating incoming wave energy and reducing coastal embankment erosion through laboratory-scale experimentation and numerical modeling. A comparative investigation between control and mangrove-protected embankment configurations under identical hydrodynamic loading was performed in a wave flume facility at Texas A&M University, Galveston. Artificial mangroves replicated characteristics of *Rhizophora mangle* (red mangrove) at a 1:15 geometric scale, incorporating trunk-root systems in staggered arrangements. Progressive wave cycles simulated storm intensification by increasing wave parameters. Free surface elevation was monitored using capacitance-type wave gauges, while laser scanning systems measured the temporal evolution of the embankment profile. Numerical validation was conducted using FLOW-3D® HYDRO with multi-physics modeling including turbulence, sediment transport, and wave-structure interaction components. Results demonstrate that mangrove-protected configurations achieved wave height reductions of 16-45% compared to 8-18% in control scenarios, with maximum energy dissipation reaching 44% under optimal wave-mangrove interaction conditions. Transmission coefficient analysis showed higher energy dissipation performance throughout all experimental cycles. Embankment erosion analysis revealed a 45% reduction in embankment erosion during optimal conditions, when wave crests achieved complete interaction with the submerged root system. However, effectiveness decreased when elevated water levels allowed wave propagation above the effective root zones. Profile evolution analysis revealed distinct morphological responses, with mangrove-protected embankments exhibiting concentrated pivot points and proximal sandbar formation, indicating enhanced energy dissipation and reduced wave reflection compared to unprotected configurations. Numerical modeling reproduced wave transformation characteristics but revealed limitations in capturing complex morphological processes due to the absence of unsaturated soil mechanics parameters in current sediment transport formulations. The findings demonstrate that nature-based artificial mangrove systems effectively enhance coastal embankment resilience through wave

energy attenuation, offering a viable solution for protecting transportation infrastructure. The submergence-dependent performance characteristics highlight the critical importance of design optimization for relative positioning between wave energy and vegetation architecture. These results provide essential foundations for developing practical implementation guidelines for artificial mangrove systems in coastal protection applications.

Keywords: Artificial Mangrove Systems, Coastal Protection, Wave Attenuation, Embankment Erosion, Transportation Infrastructure, Nature-Based Solutions

Table of Contents

List of Figures

List of Tables

INTRODUCTION

Vulnerability of Coastal Transportation Infrastructure

Coastal transportation infrastructure represents a critical component of modern socioeconomic systems, facilitating commerce, tourism, and community connectivity in coastal regions worldwide. Highway embankments, bridges, rail corridors, and port facilities located along the coastal front face severe challenges from coastal erosional processes as a consequence of the increasing frequency and magnitude of extreme weather events (Sweet et al., 2017; Dawson et al., 2018). The coastal infrastructures are vulnerable due to their direct exposure to wave action, storm surge events, and accelerated sea-level rise, which collectively threaten the structural integrity and functionality of these structures.

Among coastal transportation networks, highway corridors are particularly vulnerable to frequent disruptions from coastal hazards, resulting in increased maintenance requirements, service interruptions, and reduced asset longevity. The Federal Highway Administration (FHWA) estimates that approximately 60,000 miles of coastal highways throughout the United States are vulnerable to storm surge inundation and wave-induced damage. Hurricane-related events on coastal transportation networks have resulted in multi-billion-dollar damage to coastal roads and bridges, which are projected to escalate significantly as sea-level rise and storm intensification continue (Douglass et al., 2014).

Traditional Coastal Protection Solutions

Traditional approaches to protecting coastal transportation infrastructure have relied predominantly on hard engineering solutions, including revetments, seawalls, riprap placement, and geotextile installations (Coastal Engineering Research Center (US), 1973). While conventional methods provide immediate protection against wave forces, they present substantial limitations, including high initial costs, intensive maintenance requirements, and environmental disruption (Linham & Nicholls, 2010). Furthermore, hard engineering structures often generate adverse effects, including wave reflection, altered sediment transport patterns, and accelerated erosion in adjacent unprotected areas, creating cascading infrastructure vulnerability issues (Burcharth et al., 2010).

Acknowledging the constraints of traditional solutions, numerous coastal regions have integrated soft engineering solutions alongside conventional hard infrastructure. These nature-based systems include ecological features, such as mangrove forests, coral reefs, salt marshes, and oyster reef formations, to achieve wave attenuation and shoreline stabilization (Morris et al., 2018). While these natural solutions demonstrate considerable benefits and enhanced cost-effectiveness relative to conventional alternatives, their implementation remains constrained by several factors, including biogeographical limitations, climate sensitivity, and extended establishment periods required to achieve optimal protective functionality (Amos & Akib, 2023).

The inherent limitations of both conventional and nature-based protection systems have led to an increasing focus on innovative hybrid coastal protection solutions in research. These integrated approaches offer solutions that work in synergy with natural coastal processes, providing effective wave attenuation and shoreline stabilization (Sutton-Grier et al., 2015; Libby et al., 2024). By strategically combining the advantageous characteristics of hard and soft engineering systems, hybrid solutions minimize the respective limitations of each approach through integrated design frameworks that enhance overall system performance and long-term resilience.

Natural Mangrove Systems

Natural mangrove ecosystems have demonstrated the ability to provide coastal protection through complex hydrodynamic interactions that effectively attenuate wave energy, reduce storm surges, and stabilize sediment movements (Alongi, 2008) (Figure 1). The protective mechanisms of mangrove forests function through several processes, including drag on aerial and submerged vegetation components, energy dissipation through turbulent mixing, increased bottom friction, and sediment trapping (Mazda et al., 1997; Quartel et al., 2007). Field measurements and analytical studies have consistently documented substantial reductions in wave height as waves propagate through mangrove forests, with attenuation efficiency strongly dependent on vegetation density, forest width, submergence ratio, and incident wave characteristics (Brinkman et al., 1997; Mazda et al., 2006; Quang Bao, 2011). Figure 2 shows the percentage decrease in wave height across different wave types over a 328 ft. (100 m) mangrove forest.

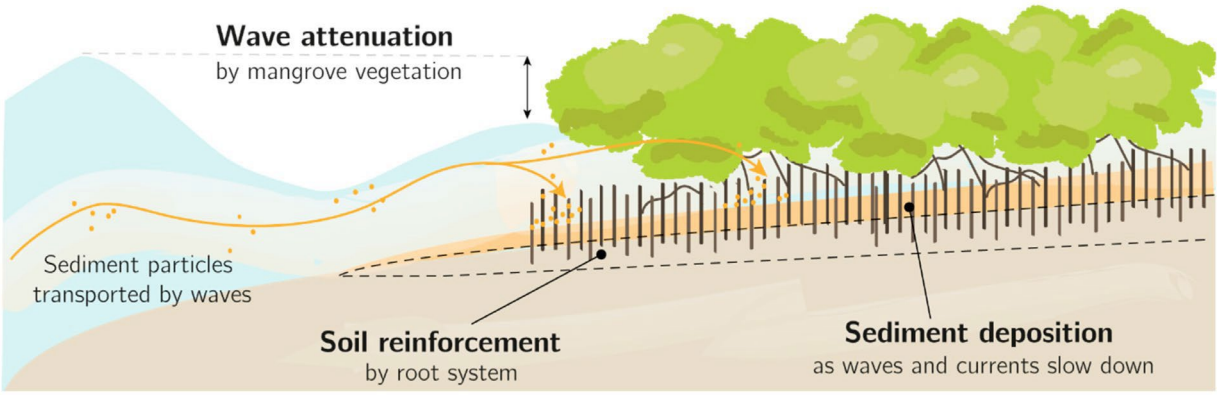

Figure 1. Protective functions of mangrove forest. *"Reprinted with permission from Gijón Mancheño et al., 2024, Spring Nature"*

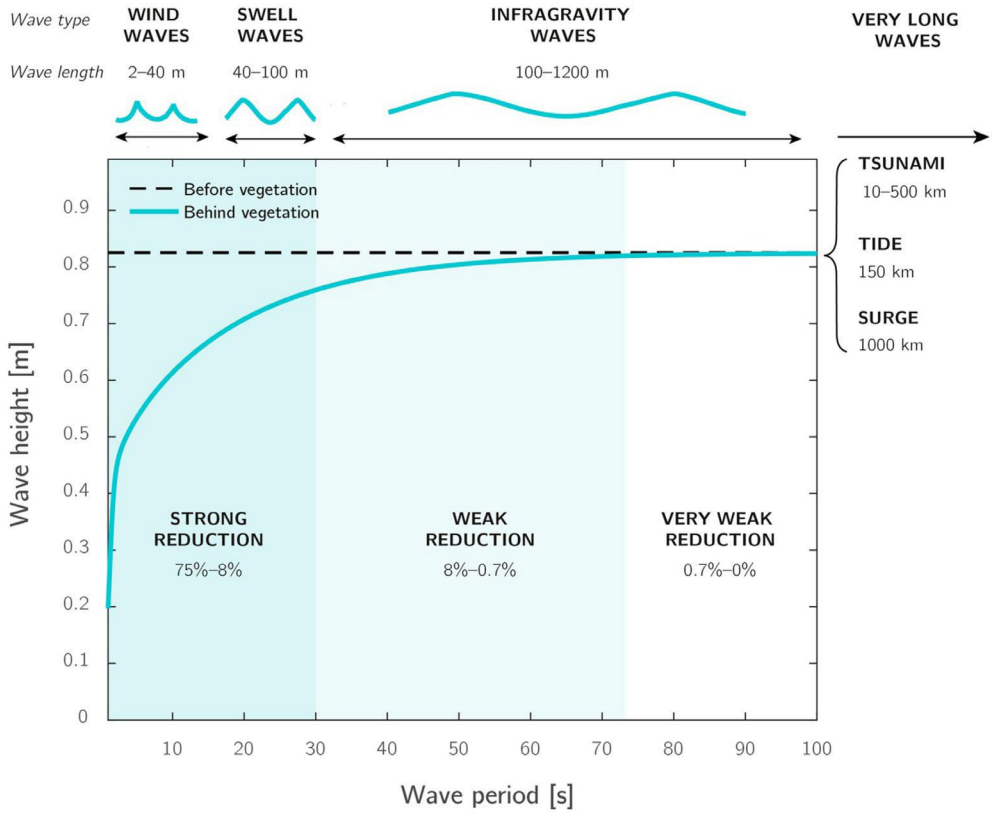

Figure 2. Wave height reduction across various types of waves over a 328 ft. (100 m) wide mangrove forest. *"Reprinted with permission from Gijón Mancheño et al., 2024, Spring Nature"*

Rhizophora mangle, also known as red mangroves, effectively dissipates wave energy through complex hydrodynamic interactions between its roots and the incoming wave (Figure 3). The roots maximize the surface area for hydrodynamic interaction while providing structural stability against incoming waves. The prop-root system of red mangroves produces substantial

drag on incoming waves. Simultaneously, the complex root increases bottom roughness and energy dissipation by causing turbulent flow separation and the formation of vortices. Additionally, the aerial root helps reduce wave energy during high water conditions, expanding the protective zone vertically and offering multi-level energy dissipation. (Mazda et al., 1997; Vo-Luong & Massel, 2008).

Figure 3. *Rhizophora mangle* (red mangrove). *Source:* https://oceaninfo.com/plants/red-mangrove/

Storm surge attenuation is another critical protective role of mangrove ecosystems, with recorded surge height reductions of 13-32 in. per mile (20-50 cm per kilometer) of mangroves during major hurricane events (K. Zhang et al., 2012). Surge reduction happens through the transfer of momentum from moving water to vegetation structures, increasing bottom friction, and flow obstruction, which together slow down surge velocity and reduce maximum surge heights near the coastline. The combination of wave attenuation and surge reduction offers comprehensive protection against the compound flooding hazards that present the greatest threats to coastal transportation infrastructure.

Another key benefit of mangrove systems is their ability to stabilize sediment. Sediment stabilization in mangrove environments helps provide long-term coastal protection by encouraging better accretion and reducing sediment resuspension. The complex root system captures suspended sediments during tidal cycles and storm events, promoting accretion (Furukawa et al., 1997). While natural mangrove forests have proven effective for coastal protection, they face significant

challenges when used for transportation infrastructure. These include geographical restrictions, long development times, maintenance needs, and potential ecosystem disruption during construction. Geographic constraints limit the natural establishment of mangroves to tropical and subtropical regions with suitable salinity, temperature, and tidal conditions. Additionally, successful mangrove restoration requires extended establishment periods to reach full protective capacity, during which developing ecosystems remain vulnerable to storm damage and offer limited protection to infrastructure. (Maza et al., 2021).

Artificial Mangrove Systems

The limitations of natural mangrove implementation have driven the development of artificial mangroves that replicate the hydrodynamic advantages of natural forests while overcoming practical challenges related to infrastructure protection. Artificial mangroves are structures designed to replicate the physical characteristics of natural mangroves, including trunk-root systems, spatial arrangements, and surface textures (Chang et al., 2022). Early artificial mangrove designs primarily employed simple geometric shapes made from stiff materials, such as PVC pipes, concrete, and steel frameworks, arranged in regular patterns to mimic natural forest layouts (Zong & Nepf, 2012; Kazemi et al., 2017). While these initial designs demonstrated measurable wave attenuation abilities, subsequent research has emphasized the importance of replicating the complex three-dimensional root structure that influences energy dissipation in natural systems (Maza et al., 2019; Yin et al., 2023).

Contemporary artificial mangrove systems are fabricated using sophisticated materials and advanced manufacturing techniques, including 3D printing technologies, flexible polymer composites, and bio-inspired design optimization, to replicate the natural morphology and hydrodynamic characteristics of mangroves. These engineered systems offer distinct advantages over their natural counterparts, including immediate operational functionality upon deployment, consistent performance independent of biological variability, reduced maintenance requirements, and customizable design parameters optimized for site-specific wave conditions and environmental constraints.

Research Objectives

Implementing artificial mangrove systems for protecting transportation infrastructure has great potential to enhance coastal infrastructure resilience, overcoming the limitations of

traditional hard engineering methods and natural vegetation systems. Despite the promising potential of artificial mangrove systems for protecting transportation infrastructure, a comprehensive understanding of their effectiveness remains limited. Previous investigations have mainly examined wave transmission in simplified mangrove models, but they have lacked a focus on complex interactions involving artificial vegetation, natural sediment transport, and infrastructure response. This knowledge gap hinders widespread adoption and calls for systematic experiments to develop clear design guidelines and performance expectations for real-world use. Therefore, the report focuses on two principal objectives:

1. Understand and investigate how wave height reduction and energy dissipation occur in artificial mangrove systems and determine the optimal conditions for enhancing the protective effects of wave-mangrove interactions through experimental and numerical methods.
2. Understand and investigate how artificial mangrove systems affect the performance of coastal transportation infrastructure, especially coastal highway embankments, by studying erosion patterns, profile changes, and morphological adjustments of the structure through experimental and numerical methods.

Report Organization

This report is organized into four primary sections:

Chapter 1 presents an introduction to the overall research topic, provides an overview of the research objectives, and outlines the structure of the report.

Chapter 2 presents a review of existing literature on mangrove systems and their applications in coastal protection.

Chapter 3 outlines the experimental methodologies used throughout the research study.

Chapter 4 outlines the numerical methodologies used throughout the research study.

Chapter 5 presents the experimental and numerical findings, including a thorough analysis and discussion of the results.

Chapter 6 provides a summary and conclusions of the research work conducted in this study, followed by recommendations for future research activities.

LITERATURE REVIEW

Laboratory Studies

Simple Cylindrical Models

Previously, artificial mangroves were implemented using simple cylindrical configurations constructed from rigid materials, such as polyvinyl chloride (PVC) piping, reinforced concrete, timber, and steel framework systems, designed to replicate natural forest spatial arrangements. Numerous researchers have employed cylindrical geometries to examine different parameters, including hydrodynamic flow attenuation, sediment transport dynamics, wave energy dissipation, and wake formation characteristics.

Nicolle & Eames, (2011) conducted a comprehensive numerical analysis of flow dynamics downstream of circular cylindrical arrays. The researchers modeled a patch by varying the number of cylinders within each patch to vary the void fraction (low – < 0.05, intermediate – 0.05 to 0.15, and high – > 0.15). Chen et al., (2012) conducted an experimental investigation to examine the influence of patch diameter (5 – 42 cm) and patch density (5.6 – 101 m^{-1}) on wake formation patterns downstream of circular arrangements of rigid wooden cylinders. However, their study did not incorporate the effects of structural flexibility on flow-vegetation interactions.

Kazemi et al., (2017) used wooden circular cylinders as a simplified mangrove root model, which served as an appropriate approximation of the mangrove roots. The researchers investigated the fluid flow (2.3 – 11.9 cm/s) and mangrove interaction across varying parameters, including porosity (0 - 91%), spatial distribution ratios (3.5 – 6.31), and structural flexibility (2.15 – 58.07 N/mm). The findings demonstrated that vortex shedding frequency had an inverse relationship with small cylinder diameter under constant patch diameter. Furthermore, a decrease in stiffness resulted in increases in both patch drag coefficients and wake deficit magnitudes downstream of the vegetation patch.

Li et al., (2022) conducted a comprehensive numerical investigation examining scour mitigation strategies for monopile foundations through the implementation of bio-inspired cylindrical skirt configurations. The study evaluated the effectiveness of mangrove-inspired protection systems by parametrically varying the ratio of submerged height to monopile diameter (0.5 – 3.0), inter-cylinder spacing, and the number of protective rings surrounding the monopile. Experimental investigations showed that skirt pile surrounding monopile foundations provides a

significant reduction in local scour. The protective skirt resulted in a 65% reduction in maximum scour depth and a 90% decrease in total scour volume relative to the unprotected monopile.

Complex Mangroves Models

The inherent limitations of simplified cylindrical configurations have led to the development of biomimetic artificial mangrove systems that more accurately replicate the complex hydrodynamic properties of natural mangrove ecosystems, thereby enhancing performance efficiency. As a result, research shifted toward the development of complex geometries that incorporate structural components, including the prop root, canopy, and trunk.

Ismail et al., (2012) conducted an experimental investigation using hybrid material artificial mangrove models to examine the performance of mangroves in reducing tsunami run-up. The mangrove incorporated plastic components to replicate the canopy, while using rattan wood for the trunk. Physical models were fabricated at a 1:100 geometric scale to facilitate laboratory-scale tsunami propagation studies. Experimental findings showed that mangrove width and density exhibit significant run-up attenuation, with wider vegetation resulting in enhanced wave energy dissipation. Initial mangrove widths of 1 m achieved run-up reductions ranging from 23 – 32 % during high water conditions and 31 – 36 % during low water conditions across vegetation densities spanning 3 – 5 to 7 – 8 trees per 100 cm^2.

Strusińska-Correia et al., (2013) conducted a laboratory investigation examining tsunami wave attenuation within mangrove. The researchers developed a tree parameterization methodology that integrated both bio-mechanical and structural properties of mangrove trees, enabling the substitution of complex natural morphologies with simplified models with equivalent hydraulic resistance characteristics. The experimental setup used wire frameworks encased in clay layers and thermally hardened in ovens to fabricate both real mangroves and their parameterized forms. The tsunami attenuation experiments were performed at a geometric scale of 1:25 to investigate the protective efficacy of mangrove forest configurations. The findings revealed that bathymetry contributes to solitary wave energy attenuation through wave breaking compared to mangrove forest alone. Tsunami transmission of approximately 20% was observed across investigated flow regimes (solitary waves and tsunami bores) when examining the maximum forest width.

Maza et al., (2019) conducted an experimental investigation using an artificial *Rhizophora* mangrove forest constructed at a 1:6 geometric scale. The model incorporated PVC pipes to

represent the main trunk and aluminum rods to simulate the characteristic prop roots of the *Rhizophora* species. Wave attenuation analysis highlighted the importance of incorporating flume boundary effects, specifically bottom and wall friction. Failure to account for these can result in significant overestimation of wave dissipation capacity. Additionally, water depth corresponding to the mangrove frontal area, and incident wave height are the primary parameters governing the effectiveness of wave attenuation for short-period waves.

Field Studies

Mazda et al., (1997) conducted field investigations in the Tong King Delta, Vietnam, within a mangrove reforestation area dominated by *Kandelia candel* specimens of different ages. At sites with sufficiently mature mangrove canopies, wave height reduction rates reached 20% per 100 m of mangrove forest width. The researchers projected that six-year-old mangrove trees could attenuate wave heights from 1.0 m to 0.05 m across a 1.5 km forest width.

Quartel et al., (2007) performed field observations in the Red River Delta, Vietnam, within mangrove communities comprising 88.9% *Kandelia candel*, 7.4% *Sonneratia* spp., and 3.7% *Avicennia marina*. Their findings showed that wave height reduction by mangroves was 5 – 7.5 times greater than just attenuation through bottom friction.

Quang Bao, (2011) investigated wave attenuation at two Vietnamese coastal mangrove sites. Results demonstrated exponential decay of wave height with increasing distance from the mangrove forest edge. The study derived a mangrove forest index incorporating tree height, density, and canopy closure parameters to determine optimal mangrove band width requirements for effective coastal protection applications. Table 1 presents a comprehensive synthesis of experimental, numerical, and field investigations examining mangrove hydrodynamics and performance.

Table 1: Review of experimental and numerical studies on mangrove hydrodynamics.

Authors	Type of Study	Hydrodynamic Conditions	Scale	Mangrove Species	Mangrove Representation	Material Used
Mazda et al., (1997)	Field	-	-	*Kandelia candel*	-	-
Quartel et al., (2007)	Field	-	-	*Kandelia candel* *Sonneratia* *Avicennia marina*	-	-
Fatimah et al., (2008)	Numerical	Regular Wave	-	-	Porous Media	-
Nicolle & Eames, (2011)	Numerical	Unidirectional Flow	-	-	Cylindrical	Rigid
Quang Bao, (2011)	Field	-	-	*Rhizophora* *Sonneratia caseolaris* *S. griffithii*	-	-
Chen et al., (2012)	Experimental	Unidirectional Flow	-	-	Cylindrical	Rigid
Ismail et al., (2012)	Experimental	Solitary Wave	1:100	*Rhizophora*	Complex	Plastic Wood
Strusińska-Correia et al., (2013)	Experimental	Solitary Wave	1:20	*Rhizophora*	Cylindrical	Wireframe Incased in Clay
Maza et al., (2015)	Numerical	Solitary Wave	-	-	Cylindrical	Rigid
Zhang et al., (2015)	Experimental	Unidirectional Flow	1:7.5	*Rhizophora*	Complex	Aluminum
Kazemi et al., (2017)	Experimental	Unidirectional Flow	-	*Rhizophora*	Cylindrical	Wood
Maza et al., (2017)	Experimental	Unidirectional Flow	1:12	*Rhizophora*	Complex	Acrylic Brass
Hoque et al., (2018)	Experimental	Regular Wave Irregular Wave	1:25	*Rhizophora*	Cylindrical	Hardened Clay
Maza et al., (2019)	Experimental	Regular Wave Irregular Wave	1:6	*Rhizophora*	Complex	PVC Aluminum
Tomiczek et al., (2020)	Experimental	Solitary Wave Regular Wave Irregular Wave	1:16	*Rhizophora*	Complex	PVC Steel

(Chang et al., 2022)	Experimental	Regular Wave Solitary Wave	1:7	*Rhizophora*	Complex	3D Printed PLA
Li et al., (2022)	Experimental Numerical	Unidirectional Flow	-	-	Cylindrical	PVC
Yin et al., (2023)	Experimental Numerical	Solitary Wave	1:10	*Rhizophora*	Complex	PVC Aluminum
Mcmann et al., (2024)	Experimental	Regular Wave	1:8	*Rhizophora*	Complex	Brass Steel

EXPERIMENTAL FRAMEWORK

This experimental investigation was conducted to evaluate the protective effectiveness of artificial mangrove systems for coastal transportation infrastructure through systematic assessment of wave attenuation mechanisms and concurrent erosion mitigation via controlled laboratory-scale testing. A comparative analysis was conducted using two embankment configurations: an unprotected configuration and a mangrove-protected configuration subjected to identical progressive wave loading conditions. The experimental design enabled quantitative assessment of differential erosion responses and wave energy dissipation characteristics between protected and unprotected systems under identical hydrodynamic conditions. The following sections present a comprehensive description of the experimental design and methodological approaches employed in this investigation.

Material and Methods

Embankment Material, Soil Characterization, and Construction

The geotechnical properties of the embankment construction material are summarized in Table 2, while the corresponding particle size distribution curve is illustrated in Figure 4. All tests were performed in accordance with the American Society for Testing and Materials (ASTM) standards. The soil used in the study was classified as poorly graded sand with silt (SP-SM) as per the Unified Soil Classification System (USCS) classification. All laboratory testing was performed in accordance with standardized protocols established by the American Society for Testing and Materials (ASTM). Based on the Unified Soil Classification System (USCS), the material was classified as poorly graded sand with silt (SP-SM), indicating a granular soil matrix with relatively uniform particle sizes and moderate cohesive properties.

The embankment was constructed within the flume in layers, using multiple uniform lifts followed by controlled compaction to ensure a consistent density throughout the embankment, as shown in Figure 5 (a and b). Each soil lift was compacted to a target relative density of 80% using a standardized 5.5 lb (2.5 kg) impact rammer with a 30.5 cm (12 in.) drop height. The compaction sequence was repeated six times to attain the specified embankment height while maintaining uniform density, which is essential for consistent erosional response under hydrodynamic loading. The upstream and downstream embankment slopes were constructed at approximately 1.67H:1V (30°). The embankment had a height (H_e) of 0.3 m (11.8 in.), width (W_e) of 0.6 m (23.6 in.), and a

crest width (L_k) of 0.2 m (7.9 in.) as shown in Figure 5c. Following completion of embankment construction, the wave tank water level was incrementally raised until the structure achieved a half-submerged condition.

Table 2: Basic properties of the material.

Property	Units	Standard	Values
Specific gravity, G_s	Not Applicable	ASTM D854	2.65
Percentage Sand	%	ASTM D6913	91
Percentage Fines	%	ASTM D7928	9
USCS Soil Classification	Not Applicable	ASTM D2487	SP-SM
Liquid Limit	%	ASTM D4318	Non-Plastic
Plasticity Limit	%	ASTM D4318	Non-Plastic
Plasticity Index	%	ASTM D4318	Non-Plastic
Maximum Void Ratio, e_{max}	Not Applicable	ASTM D4254	0.90
Minimum Void Ratio, e_{min}	Not Applicable	ASTM D4253	0.60

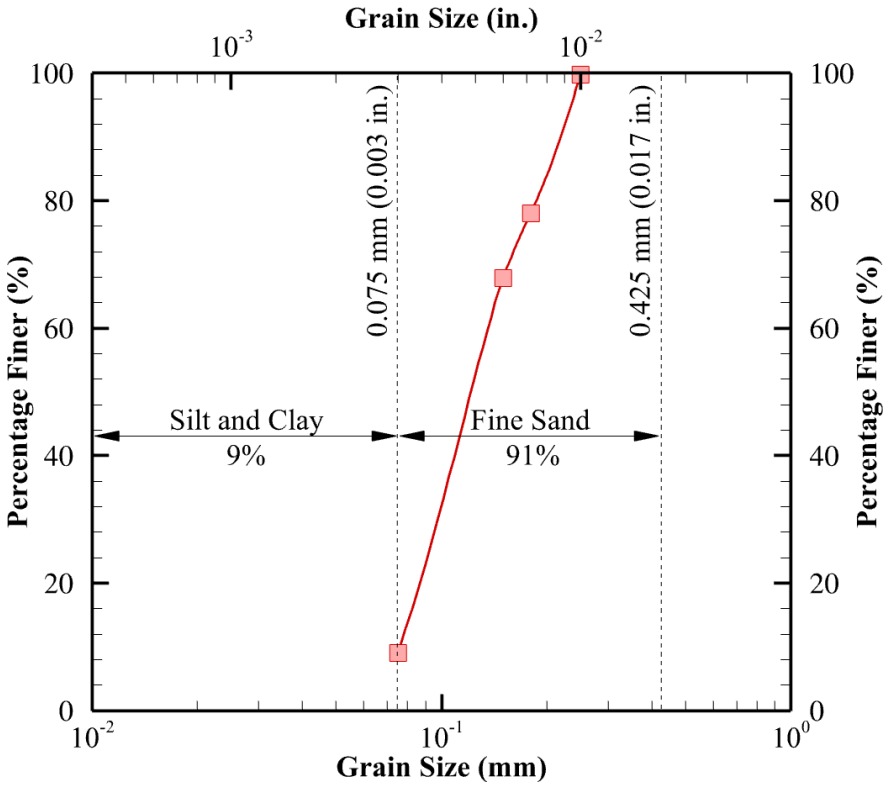

Figure 4. Grain size distribution of the soil.

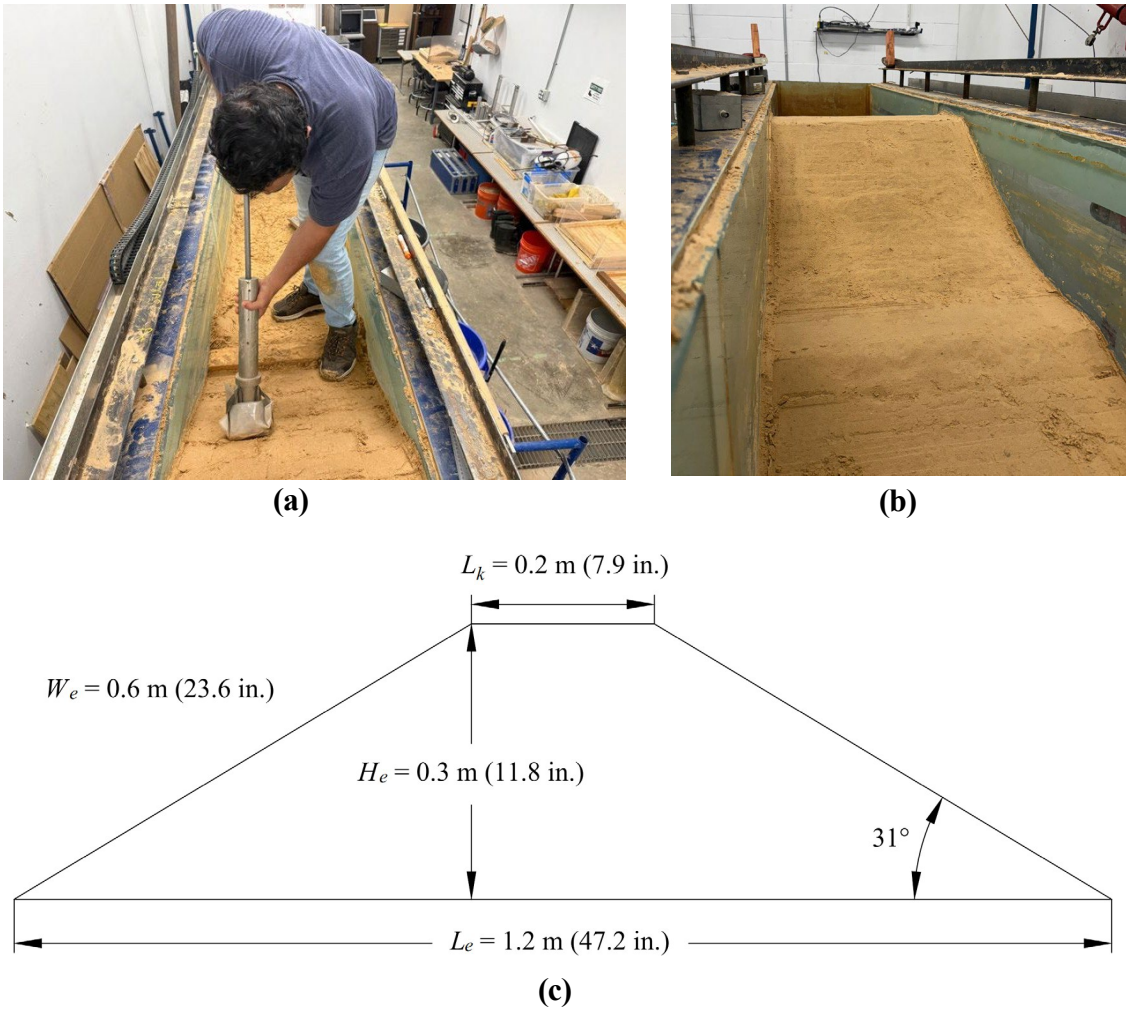

Figure 5. Construction and geometric configuration of the embankment: (a) Compaction during embankment construction within the wave flume; (b) Completed embankment structure prior to testing; (c) Dimensional specifications.

Design of Artificial Mangrove

The artificial mangroves were designed to replicate the morphological characteristics of *Rhizophora mangle* (red mangroves) native to Key West, Florida, incorporating geometric parameters derived from established field studies and previous research investigations (Strusińska-Correia et al., 2013; Maza et al., 2019; Chang et al., 2022a). The mangrove modeling followed the parametric framework established by Ohira et al., which correlates root system dimensions and spatial distribution with the main trunk diameter at breast height (DBH), providing a systematic methodology for scaling natural mangrove architecture to laboratory conditions. The biomimetic design ensures that artificial mangroves capture the essential hydrodynamic characteristics of

natural mangrove forests while enabling controlled experimental investigation of wave attenuation mechanisms.

The artificial mangrove systems were scaled to a 1:15 geometric scale to accommodate the dimensional constraints of the wave flume facility (Tomiczek et al., 2020). Figure 6a shows the dimensions of the artificial mangrove model, with a DBH of 0.02 m (0.8 in.), internal diameter of 0.01 m (0.5 in.), maximum root height (H_{R_max}) of 0.15 m (5.9 in.), root spread distance (x) of 0.3 m (11.8 in.), and individual root diameter (ϕ_R) of 0.006 m (0.3 in.). The trunk component was fabricated using polyethylene terephthalate glycol (PETG) material. At the same time, the root system was constructed using cross-linked polyethylene (PEX) pipe to provide the necessary flexibility and durability under hydrodynamic loading. The roots were installed through 45° spiral holes along the trunk with 1.3 cm (0.5 in.) vertical spacing, incorporating 11 individual roots configured in a parabolic curvature. A total of 30 artificial mangrove units were manufactured and placed in the experimental setup, as shown in Figure 6 (b and c). The mangrove array consisted of two panels with combined dimensions of 1.8 m (70.9 in.) length and 0.6 m (23.6 in.) width, positioned 1.2 m (47.2 in.) seaward from the upstream embankment toe. Individual mangroves were arranged in a staggered spatial configuration with 0.17 m (6.7 in.) inter-specimen spacing (Δs), with a vegetation density (N) of 40 trees/m^2 calculated according to the equation below.

(1)

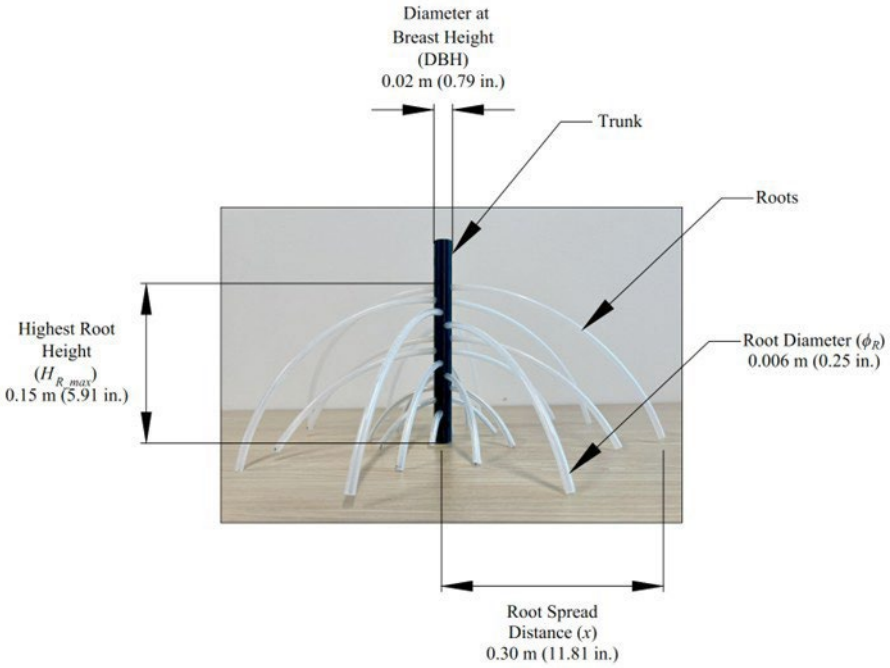

(a)

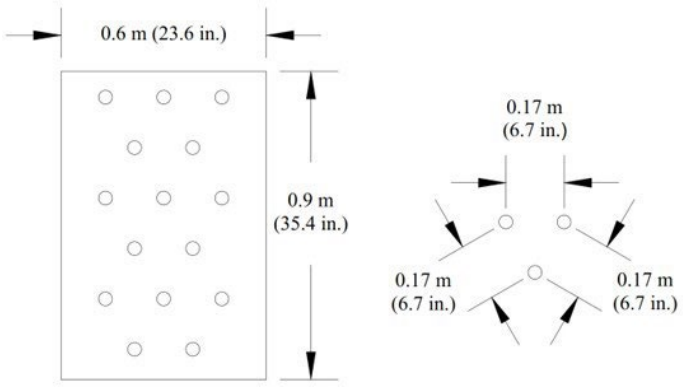

(b)

(c)

Figure 6. Construction and geometric configuration of the artificial mangroves: (a) Dimensional specifications; (b) Arrangement of mangroves; (c) Mangroves placed in wave flume prior to testing.

Experimental Setup

Flume Test

The experimental investigations were conducted at the ocean engineering laboratory of Texas A&M University, Galveston (TAMUG), Texas, USA, utilizing a wave flume facility with dimensions of 15.0 m (49.2 ft.) in length, 1.2 m (3.9 ft.) in height, and 0.6 m (2.0 ft.) in width. Figure 7 presents a cross-sectional schematic of the experimental flume configuration used in this investigation. Wave generation was achieved through an electrically operated flap-type wave maker system capable of producing both regular and irregular wave conditions, with operational control managed via computer software from a centralized control station. The wave generator was positioned in the deeper section of the flume, seaward of the embankment structure. A wave-absorbing mesh was placed behind the wave generator to minimize sloshing and wave reflection effects that could compromise wave generation accuracy (Hughes, 1993). The flume base was elevated 0.3 m (1.0 ft) through the installation of a false floor system, which served as the foundation for embankment construction. This false floor incorporated a 7H:1V slope to facilitate a gradual bathymetric transition from the deep-water zone to the shallow-water region, replicating realistic nearshore profile conditions. The shallow-water region had a very gentle bathymetric slope of 50H:1V, extending to the embankment toe, which provided realistic nearshore conditions for wave transformation and shoaling processes. The artificial mangrove array was positioned 1.2 m (3.9 ft.) seaward from the embankment toe.

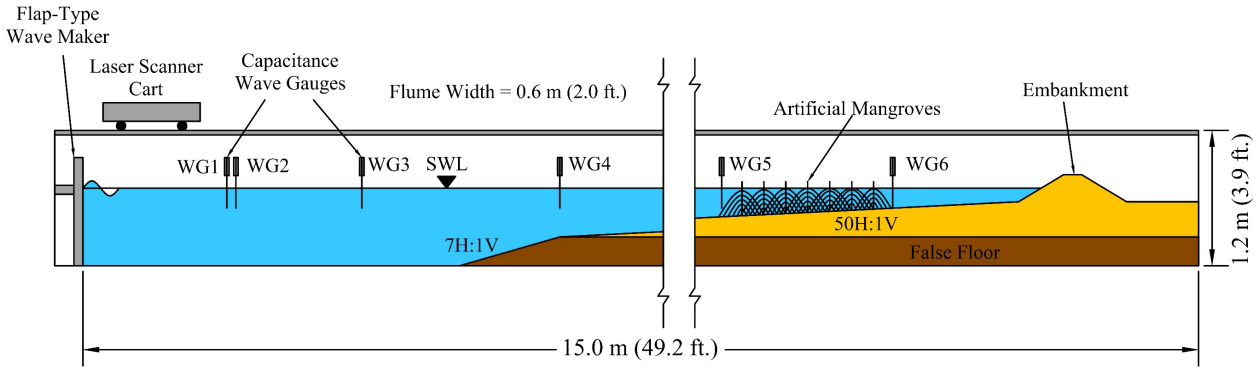

Figure 7. Cross-section of experimental wave flume setup.

Instrumentation, Calibration, and Data Analysis

In wave flume experimentation, continuous monitoring of free surface elevation (η) throughout the flume length is essential to verify that generated wave characteristics correspond

to specified target parameters and ensure experimental accuracy. To achieve this, six capacitance-type wave gauges (WGs) were installed along the flume length to capture the spatial transformation of waves. The wave measurement system consisted of individual wave probe heads coupled with signal conditioning units, as illustrated in Figure 8 (a and b). The wave gauges (WG1–WG6) were positioned at longitudinal distances of 1.6 m (5.2 ft.), 1.7 m (5.6 ft.), 3.1 m (10.2 ft.), 5.2 m (17.1 ft.), 9.6 m (31.5 ft.), and 11.5 m (37.7 ft.) from the wave generator, as shown in Figure 7, allowing for tracking wave propagation and transformation throughout the experimental domain. All wave gauges operated at a sampling frequency of 20 Hz, providing sufficient temporal resolution.

(a) **(b)**

Figure 8. Free surface elevation (η) measurement system: (a) Wave probe; (b) Wave gauge box.

WG1 served as the reference for calibrating the remaining wave gauges, as the raw voltage output required conversion to centimeters for accurate measurement of water surface elevation. Wave gauge calibration was performed using a step-down method (Hughes, 1993). The flume was initially filled to a reference water depth of 95.0 cm (3.1 ft.), establishing a stable baseline condition for calibration measurements. The partially submerged WG1 was then incrementally lowered in 1.0 cm (0.4 in.) intervals while recording ten voltage measurements at each position. Subsequently, the water level was reduced while maintaining continuous measurement acquisition during the drainage process to capture the complete range of operational water levels. Upon

completion of the calibration sequence, linear regression analysis was performed to establish the calibration relationship, providing voltage-to-elevation conversion by the equation below:

(2)

where the coefficient a represents the gauge sensitivity and b denotes the offset parameter. The slope coefficient provides the conversion factor for transforming voltage readings to centimeter units across all wave gauges. Figure 9 presents the calibration plots and corresponding conversion factors for all wave gauges used in the experimental investigation.

The raw wave elevation data acquired from the wave gauges were preprocessed to remove the mean water level and center the measurements around zero elevation through detrending. The detrending procedure was implemented using the mathematical relationship presented below:

(3)

where $\eta'(t)$ is the detrended wave elevation, $\eta(t)$ is the original wave elevation, and $\overline{\eta}$ is the mean elevation over the entire record. Data analysis of each water surface elevation time series incorporated the zero-upcrossing methodology to extract individual regular wave heights (H) from the continuous measurement. The zero-upcrossing technique defines an individual wave as the signal segment between two consecutive points where the detrended water surface elevation transitions upward through the mean water level (zero reference line). The zero-upcrossing was identified through a search algorithm that identified transitions from negative to positive elevation values within the detrended data. Figure 10 shows the wave identification process applied to a representative water surface elevation time series, where the blue dashed line represents the complete measured signal and the red solid line indicates the selected subsample used for wave height analysis. The initial 5 s was eliminated from the analysis to take account of the wave ramp-up effect.

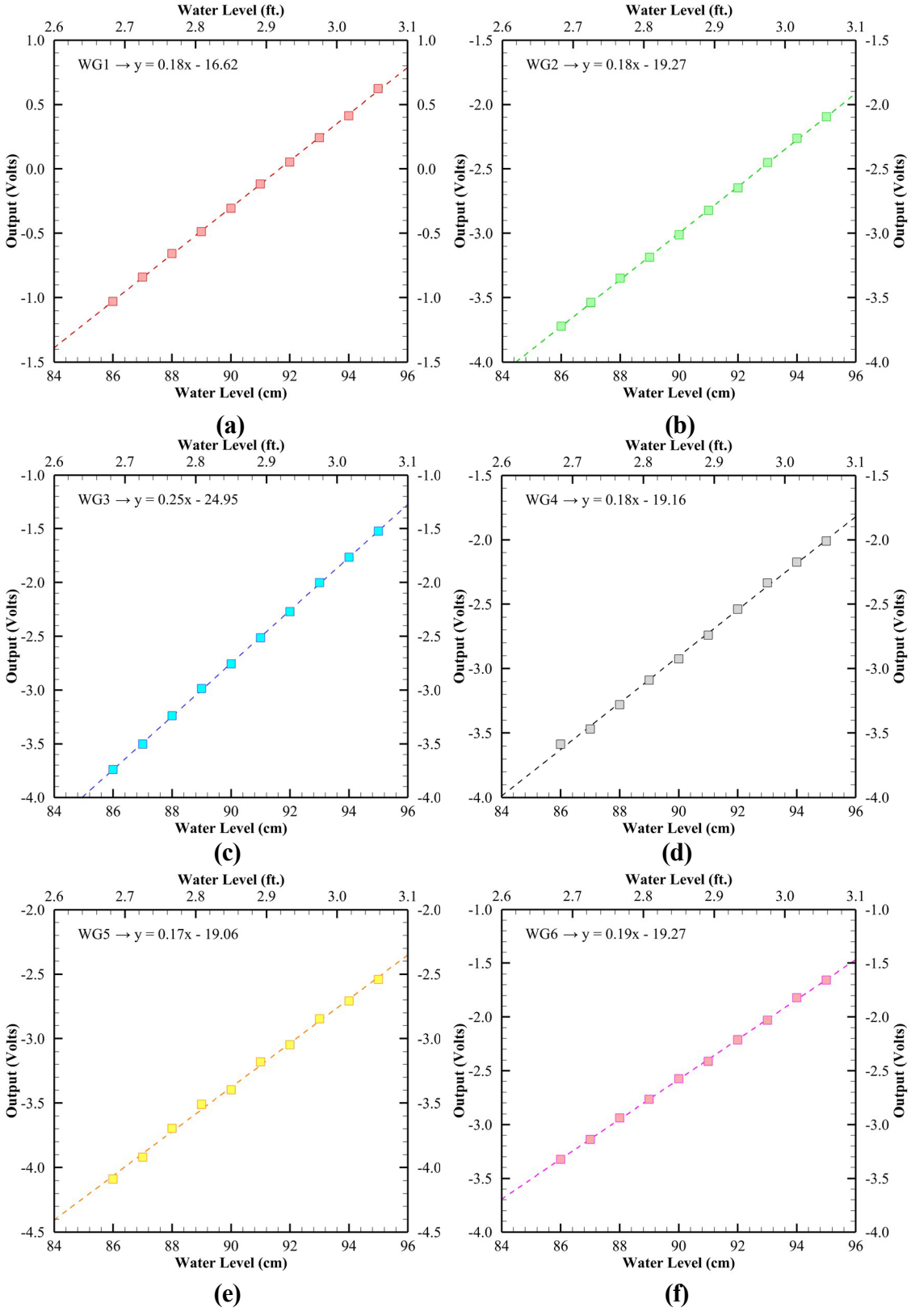

Figure 9. Wave gauge calibration: (a) WG1; (a) WG2; (a) WG3; (a) WG4; (a) WG5; (a) WG6.

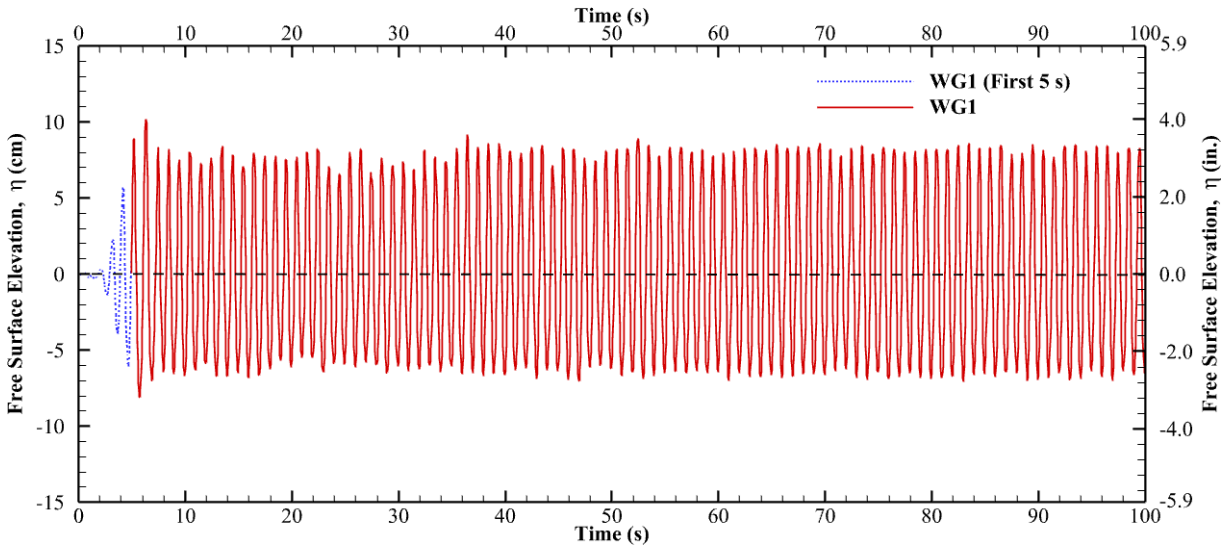

Figure 10. Detected waves from the full-time series.

The significant wave height ($H_{1/3}$), defined as the average height of the highest one-third of waves within the measurement record, was computed using the mathematical formulation presented below after sorting the individual wave heights in descending order:

(4)

where in the sorted array of wave heights, $N_{1/3}$ represents the number of waves in the highest one-third ($N_{1/3} = N/3$), and H_i represents the individual wave heights.

Laser Line Scanner

Wave action on the upstream embankment slope initiates erosional processes that result in continuous temporal modification of the embankment profile. A laser line scanning system was used to monitor the evolution of the embankment profile throughout the experimental duration, providing high-resolution measurements of morphological changes. The laser scanner was mounted on a horizontally translatable cart system positioned above the flume facility, enabling comprehensive spatial coverage of the embankment profile, as illustrated in Figure 11a. The measurement system incorporated a high-power blue laser diode operating at 540 nm (2.1×10^{-5} in.) wavelength coupled with a 200 Hz two-dimensional charge-coupled device (CCD) detector for determining lateral and vertical dimensions (y and z directions), while a red laser was utilized for longitudinal measurements (x direction), as shown in Figure 11b. The blue laser diode

generated an alongshore-oriented laser line projected vertically onto the embankment and surrounding surface, creating a reference plane for elevation determination. The CCD detector captured reflected laser radiation and computed elevation measurements with millimeter precision by analyzing the reflected light intensity, providing accurate quantification of surface topography (Figlus et al., 2014). During experimental procedures, the cart system traversed at sufficiently reduced velocities to ensure measurement accuracy while avoiding distortions that could compromise data quality. Prior to each profile scanning sequence, the surface was verified to be free of standing water, as surface moisture can compromise measurement validity by interfering with laser light reflection and causing erroneous elevation calculations.

Wave Test Conditions

This investigation employed regular wave conditions in the laboratory wave flume, characterized by monochromatic sinusoidal waves exhibiting constant wave height and period parameters that propagate uniformly without temporal variation in amplitude or frequency characteristics (Dean & Dalrymple, 1991). The experimental program was designed to simulate progressive storm intensification through systematic escalation of wave energy conditions over time. The experimental program consisted of 10 sequential wave cycles with systematically increasing wave intensity to replicate the temporal evolution of storm conditions. This approach simulates realistic storm scenarios where wave conditions intensify gradually, allowing assessment of cumulative damage processes and morphological adjustment patterns under evolving hydrodynamic conditions. The initial eight wave cycles were limited to 5 min to minimize effects from sloshing and wave reflection within the confined flume. The final two wave cycles were extended to 10 min as wave reflection effects diminished substantially due to the progressively gentler embankment profile configuration that developed through erosional processes during earlier cycles. The total experimental duration was 60 min, providing sufficient time for significant morphological development while maintaining controlled laboratory conditions. Target wave parameters for all experimental cycles are presented in Figure 12 and Table 3, documenting the progression of wave heights, periods, and water depths throughout the testing sequence. Wave conditions were systematically intensified throughout the test sequence to replicate storm progression and promote continued embankment erosion, as morphological equilibrium tends to develop after prolonged exposure to constant wave conditions, resulting in negligible further erosion (Ozeren et al., 2021).

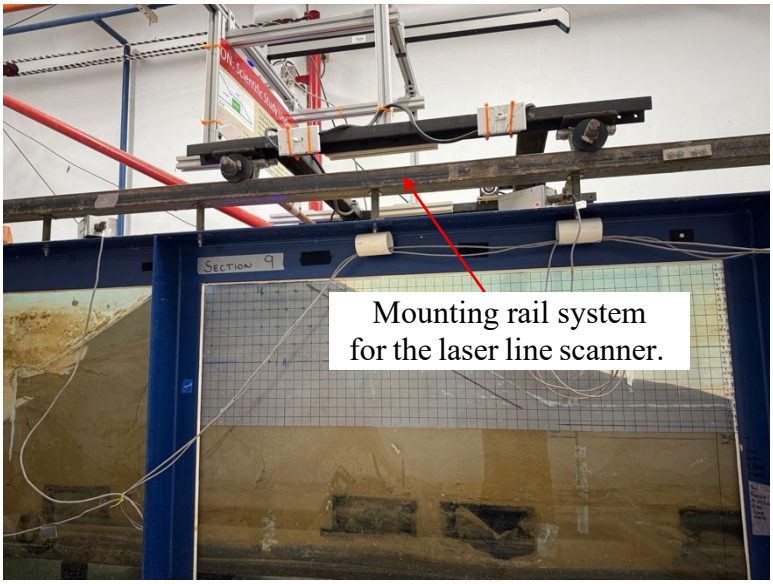

(a)

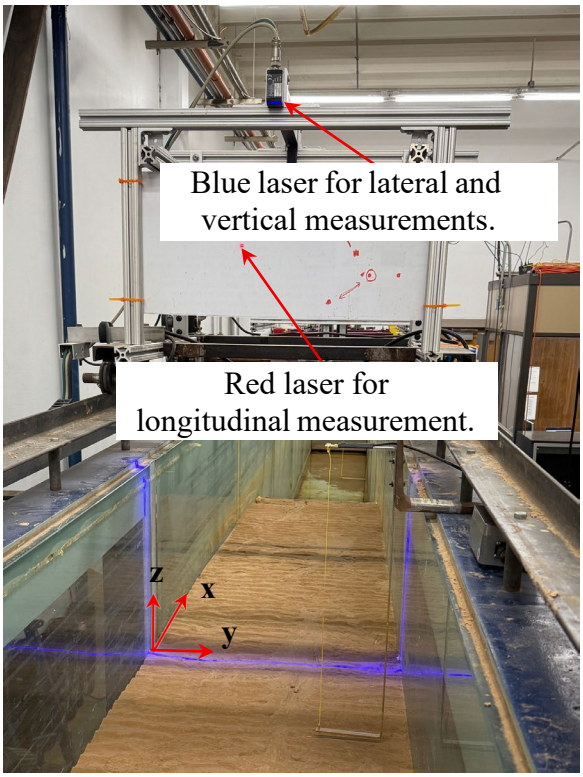

(b)

Figure 11. Laser line scanning system for embankment profile measurement: (a) Rail system for horizontal translation of the laser cart assembly, (b) Multi-laser configuration for comprehensive three-dimensional profile monitoring.

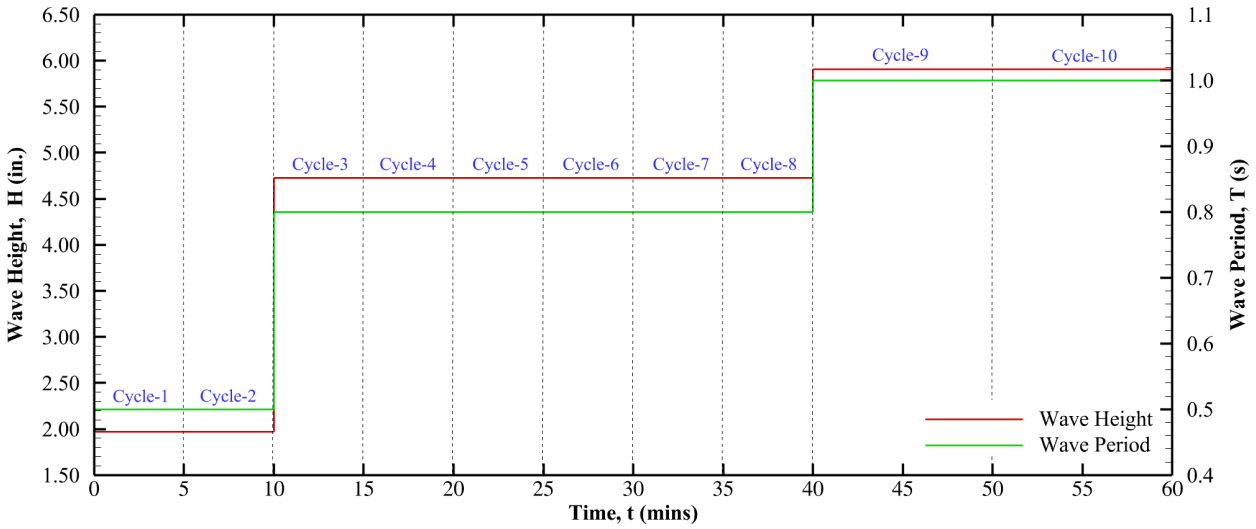

Figure 12. Wave test conditions transformation.

Table 3. Wave test parameters used in the experiment.

Wave Cycle	**Wave Height (*H*) m (in.)**	**Water Depth (*d*) m (in.)**	**Wave Period (*T*) s**	**Wavelength (*L*) m (in.)**
Cycle 1	0.05 (1.96)	0.95 (37.40)	0.50	0.39 (15.35)
Cycle 2	0.05 (1.96)	0.95 (37.40)	0.50	0.39 (15.35)
Cycle 3	0.12 (4.72)	0.95 (37.40)	0.80	1.00 (39.37)
Cycle 4	0.12 (4.72)	0.95 (37.40)	0.80	1.00 (39.37)
Cycle 5	0.12 (4.72)	0.95 (37.40)	0.80	1.00 (39.37)
Cycle 6	0.12 (4.72)	1.00 (39.37)	0.80	1.00 (39.37)
Cycle 7	0.12 (4.72)	1.00 (39.37)	0.80	1.00 (39.37)
Cycle 8	0.12 (4.72)	1.00 (39.37)	0.80	1.00 (39.37)
Cycle 9	0.15 (5.90)	1.00 (39.37)	1.00	1.56 (61.42)
Cycle 10	0.15 (5.90)	1.00 (39.37)	1.00	1.56 (61.42)

NUMERICAL MODELING

The numerical modeling in this investigation was performed using FLOW-3D® HYDRO (Version 2023R2; 2023; https://www.flow3d.com; Flow Science, Inc.), a specialized computational fluid dynamics (CFD) software designed for complex free-surface flow applications in hydraulic and coastal engineering. FLOW-3D® HYDRO employs the finite difference method to solve the Reynolds-Averaged Navier-Stokes (RANS) equations coupled with advanced turbulence modeling capabilities, providing robust simulation of wave propagation, wave-structure interaction, and fluid-sediment transport processes. The software incorporates the Volume of Fluid (VOF) method for accurate free-surface tracking, enabling precise representation of wave dynamics and air-water interface evolution throughout the computational domain (Hirt & Nichols, 1981).

Physics Model

The numerical simulation framework incorporated four physics models to represent the complex hydrodynamic and morphological processes governing wave-embankment-vegetation interactions: (a) gravity and non-inertial, (b) variable density flow, (c) turbulence and viscosity, and (d) sediment transport. The gravity and non-inertial model accounts for gravitational acceleration effects and forces arising from non-inertial reference frames. The gravitational acceleration component was specified as -9.81 m/s² (32.2 ft/s²) in the vertical z-direction. The variable-density flow model enables the simulation of flows characterized by spatial and temporal variations in density throughout the computational domain. The density was evaluated as a function of other quantities (e.g., temperature or scalars). The fluid properties were specified as follows: a density of 998.2 kg/m³ at 20°C (62.3 lb/ft.³ at 68°F), a compressibility of 4.6×10^{-10} Pa^{-1} (3.2×10^{-6} psi^{-1}), and a dynamic viscosity of 0.001 kg/m/s. The viscosity and turbulence model incorporates computation of viscous stress and turbulent flow quantities into the solution, providing an essential representation of energy dissipation mechanisms, boundary layer effects, and turbulent mixing. For the numerical simulation, the Renormalized Group (RNG) turbulence model was selected due to its enhanced capability to resolve complex flow phenomena (Yin et al., 2023). The sediment transport model approximates the coupled effects of hydrodynamic forces on surface erosion processes and subsequent sediment transport phenomena, incorporating both bedload and suspended load transport mechanisms. The critical Shields parameter was determined

empirically using the Soulsby-Whitehouse equation (Soulsby, 1997). Additionally, bedload transport rates were estimated using the Van Rijn equation (Van Rijn, 1984). The sediment properties implemented in the numerical simulation are presented in Table 4.

Table 4. Sediment characteristics.

Property	**Units**	**Values**
Diameter, d_{50}	mm (in.)	0.13 (5×10^{-6})
Particle Density, ρ_s	kg/m³ (lb/ft.³)	2650 (165.4)
Maximum Packing Fraction	Not Applicable	0.64
Entrainment Coefficient	Not Applicable	0.018
Bed Load Transport Model	Not Applicable	Van Rijn
Bed Load Coefficient	Not Applicable	0.053
Bed roughness/d_{50} Ratio	Not Applicable	2.5
Angle of Repose	°	35

Geometry

Figure 13 shows the geometric configuration of the embankment profile and artificial mangrove integrated into the numerical modeling domain, maintaining identical dimensional specifications to the physical experimental setup. The geometric representations were imported into the computational framework as stereolithography (STL) files. The artificial mangrove configuration was incorporated into the numerical domain as a non-deformable solid body, representing infinite structural rigidity consistent with the rigid PETG and PEX materials utilized in the physical model construction. The artificial mangrove array was located 1.2 m (3.9 ft.) from the embankment toe as described earlier. The embankment profile was defined as a packed sediment bed composed of discrete soil particles subject to entrainment and transport under hydrodynamic loading conditions.

Meshing

The numerical investigation employed a structured mesh within a Cartesian coordinate framework to discretize the computational domain. Multi-block meshing was implemented to optimize computational efficiency while maintaining appropriate spatial resolution in critical regions, as uniform mesh refinement throughout the entire domain would result in computational costs and memory requirements. The computational domain was divided into two distinct mesh blocks characterized by different spatial resolutions: a coarse mesh region and a fine mesh region (Figure 14). The embankment region was discretized using a coarse mesh with a uniform cell size

of 0.025 m (0.98 in.). Conversely, the artificial mangrove region was refined using a nested fine mesh block with a uniform cell size of 0.0025 m (0.098 in.). The complete numerical mesh comprised 10,000,800 computational cells distributed throughout the modeling domain. Mesh sensitivity analysis was performed to ensure adequate spatial resolution and verify the independence of numerical results from mesh density effects.

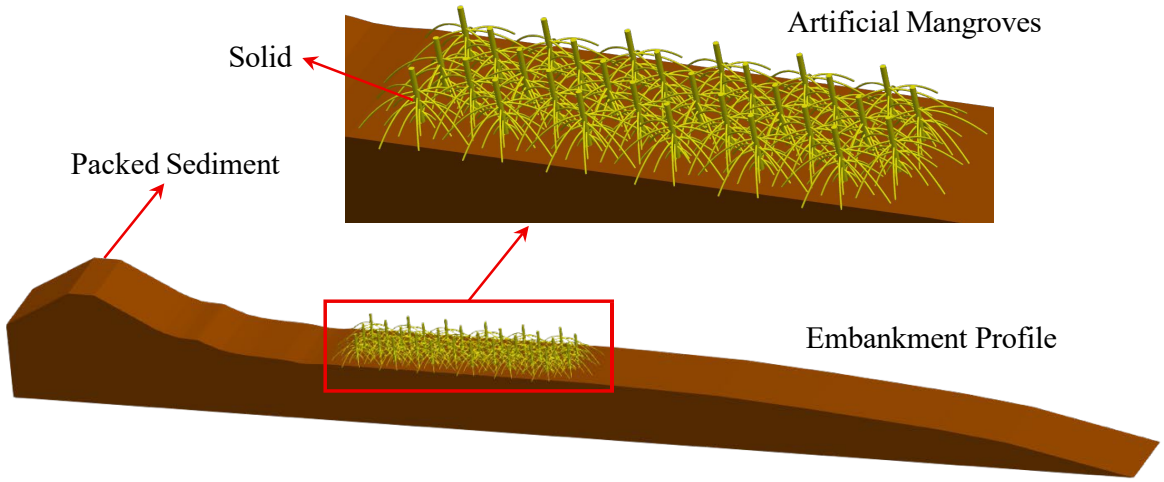

Figure 13. Numerical model of the embankment and artificial mangroves.

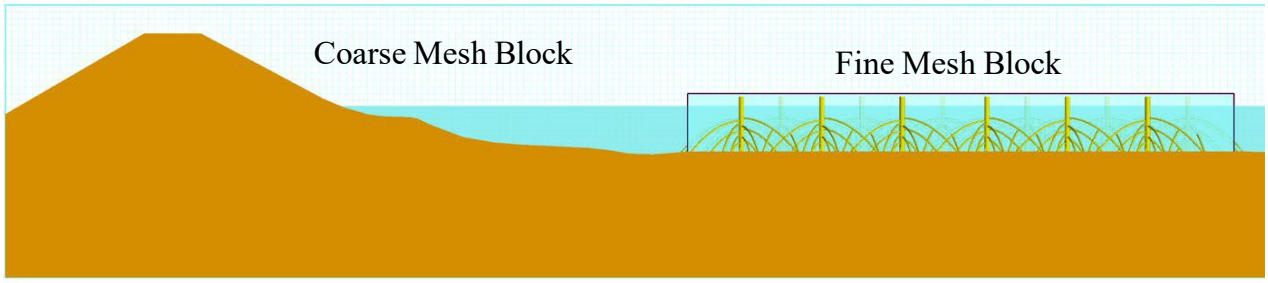

Figure 14. Multi-block nested mesh in FLOW-3D® HYDRO.

Boundary Conditions

The accurate assignment of boundary conditions is crucial to obtaining reliable and physically accurate numerical results in computational fluid dynamics simulations. Figure 15 illustrates the boundary conditions applied to the multi-block nested mesh, ensuring appropriate representation of physical constraints and flow characteristics throughout the simulation region. A total of twelve distinct boundary conditions were assigned to capture the essential physics of the wave flume environment. In the coarse mesh block, wall boundary conditions were imposed at

surfaces ABFE, DCGH, and ABCD, representing the rigid flume boundaries and ensuring no-slip velocity conditions and zero normal flow. The boundary ADHE was assigned as a pressure boundary, with the fluid elevation corresponding to the experimental water level, thereby maintaining a hydrostatic pressure distribution. Boundary BCGH was configured as a pressure boundary with zero fluid fraction to accurately simulate atmospheric conditions above the free surface, enabling a realistic representation of the air-water interface. The wave generation boundary EFGH was assigned regular wave conditions to replicate the experimental wave maker characteristics, incorporating the assumption of an infinite reservoir with uniform bathymetry external to the computational domain directly adjacent to the wave generation zone. For the nested fine mesh block encompassing the artificial mangrove region, symmetry boundary conditions were applied at surfaces IJNM, LKOP, MNOP, and IJKL, ensuring conservation of mass and momentum across block interfaces while maintaining computational continuity between mesh regions. The JKON boundary was assigned as a pressure boundary with zero fluid fraction.

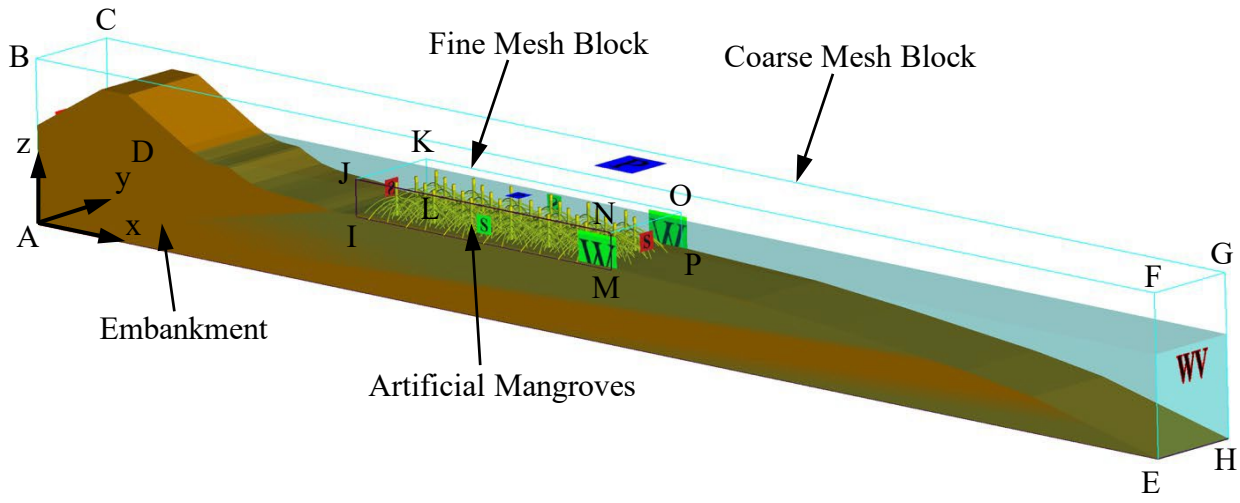

Figure 15. Boundary conditions within the numerical domain.

RESULTS AND DISCUSSION

Validation of Free Surface Elevation

Validation of numerical model accuracy requires comparison between computational and experimental measurements to ensure a reliable representation of physical phenomena. To establish this validation, free-surface elevation time series from both experimental measurements and numerical simulations were analyzed for a direct quantitative comparison for one of the cases. Figure 16 presents a comparative analysis of free surface elevation data obtained from WG4 during Cycle-3 conditions for laboratory observations and computational results. The numerical model shows agreement with experimental data, as evidenced by the close alignment of wave amplitude, frequency, and phase characteristics throughout the measurement period. The computational framework accurately captures the wave propagation and transformation processes within the experimental domain, providing confidence in the model's predictive capabilities for subsequent parametric investigations. The successful reproduction of experimental wave characteristics indicates that the selected numerical methods, boundary conditions, and physical models are appropriate for simulating the hydrodynamic processes governing wave-embankment-artificial mangrove interactions.

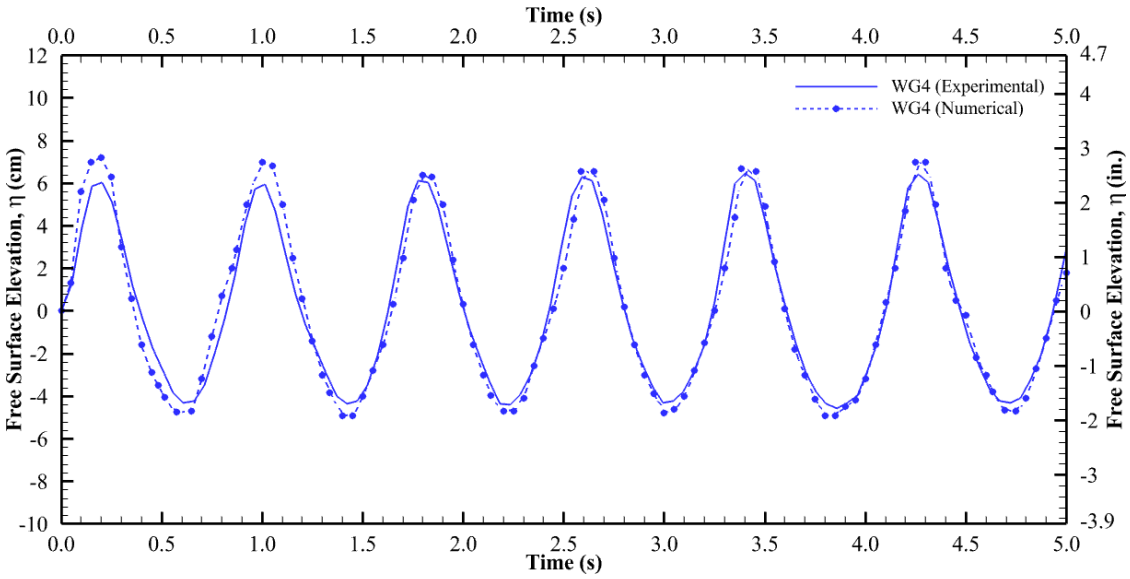

Figure 16. Validation of free surface elevation between laboratory experiment and numerical simulation for WG4 during cycle 3 with d = 0.95 m (37.4 in.).

Change in Significant Wave Height ($\Delta H_{1/3}$)

Figure 17 presents the temporal evolution of $H_{1/3}$ throughout successive wave cycles as measured by wave gauges WG4 – WG6 positioned along the flume length for both unprotected and mangrove-protected configurations. The accuracy of the numerical model was assessed by calculating the root-mean-square error (RMSE) values between the simulated and experimentally measured $H_{1/3}$ values. For the unprotected configuration, RMSE values were 0.63 cm (0.25 in.), 0.51 cm (0.20 in.), and 0.50 cm (0.19 in.) for wave gauges WG4, WG5, and WG6, respectively. The mangrove-protected configuration exhibited RMSE values of 0.45 cm (0.18 in.), 0.63 cm (0.25 in.), and 0.56 cm (0.22 in.) for the corresponding wave gauge locations, indicating agreement between computational predictions and laboratory measurements.WG1–WG3 exhibited consistent $H_{1/3}$ values across all cycles due to their proximate spatial positioning. Wave gauges positioned at increasing distances from the wave maker demonstrated systematic $H_{1/3}$ reduction due to viscous boundary layer energy dissipation and depth-limited wave breaking processes as waves propagated through progressively shallower water conditions. Wave transformation behavior was consistently observed under both unprotected and mangrove-protected configurations. Comparative analysis of Figure 17 (a and b) shows significant $H_{1/3}$ attenuation between WG5 (positioned seaward of the mangrove array) and WG6 (located landward of the mangrove array), demonstrating the effectiveness of artificial mangrove systems for wave energy dissipation. The observed $H_{1/3}$ reduction results from energy dissipation mechanisms arising from wave-mangrove interaction, supplemented by enhanced wave breaking phenomena within the vegetation zone. The drag forces exerted by the submerged root system, turbulent energy transfer and mixing within the three-dimensional mangrove canopy structure, and depth-limited wave breaking processes collectively contribute to the reduction in wave energy observed in the protected configuration.

Figure 18 presents the change in significant wave height ($\Delta H_{1/3}$) between WG5 (positioned seaward of the mangrove forest) and WG6 (positioned landward of the mangrove forest) for both unprotected and mangrove-protected configurations. For the unprotected configuration, the RMSE value was 3.45%. The mangrove-protected configuration exhibited an RMSE value of 2.81%. The unprotected configuration exhibited $\Delta H_{1/3}$ values ranging from 5% to 30%. In contrast, the mangrove-protected configuration demonstrated significant reductions in wave height, varying from 11% to 45% across cycles 1 through 10. A distinctive temporal pattern emerged in the mangrove-protected case, characterized by progressively increasing $\Delta H_{1/3}$ values through cycle 5,

followed by a decrease in subsequent cycles. During initial cycles when wave heights are small and water levels are low, incident wave crests achieve optimal interaction with the submerged root system, maximizing energy dissipation through form drag mechanisms and turbulent mixing within the vegetation canopy. Conversely, as wave heights and water levels increased in subsequent cycles, wave crests began propagating above the effective root zone, resulting in reduced wave-mangrove interaction and correspondingly diminished attenuation performance. Despite this temporal variability in protection efficiency, all mangrove-induced wave height reductions substantially exceeded those observed in the unprotected configuration, demonstrating the consistent protective capacity of artificial mangrove systems under diverse hydrodynamic conditions.

Transmission Coefficient (K_T)

An alternative methodology for quantifying wave energy dissipation and assessing the effectiveness of artificial mangrove systems in attenuating waves involves determining the transmission coefficient (K_T). The K_T is defined as the ratio of transmitted wave height (H_T) measured landward of the artificial mangrove system to the incident wave height (H_I) measured seaward of the system, as expressed in the equation below (Hoque et al., 2018). The K_T parameter ranges from 0 to 1, where unity indicates complete wave transmission with negligible energy dissipation. At the same time, zero represents the total absorption of wave energy within the protective structure.

(5)

Figure 19 presents the temporal variation in K_T across successive wave cycles for both unprotected and mangrove-protected configurations. The control case demonstrated K_T fluctuations due to wave reflection phenomena within the confined flume environment. Maximum wave energy dissipation occurred in the unprotected configuration during cycle 3, resulting in an 18% energy loss as waves propagated through the measurement section. The mangrove-protected configuration exhibited substantially enhanced energy dissipation performance, particularly during cycles 3 through 6, achieving maximum energy losses of 44%. This significant enhancement in wave energy attenuation under mangrove protection results from energy dissipation mechanisms, including form drag forces generated by the complex three-dimensional root, enhanced turbulent

mixing within the vegetation canopy, and intensified wave breaking processes induced by flow obstruction. Throughout the wave cycles, the artificial mangrove system consistently demonstrated higher energy dissipation compared to the unprotected configuration, corroborating the $\Delta H_{1/3}$ trends discussed previously. The transmission coefficient provides quantitative evidence of the substantial potential for artificial mangrove systems to reduce incident wave energies and enhance the effectiveness of coastal embankment protection.

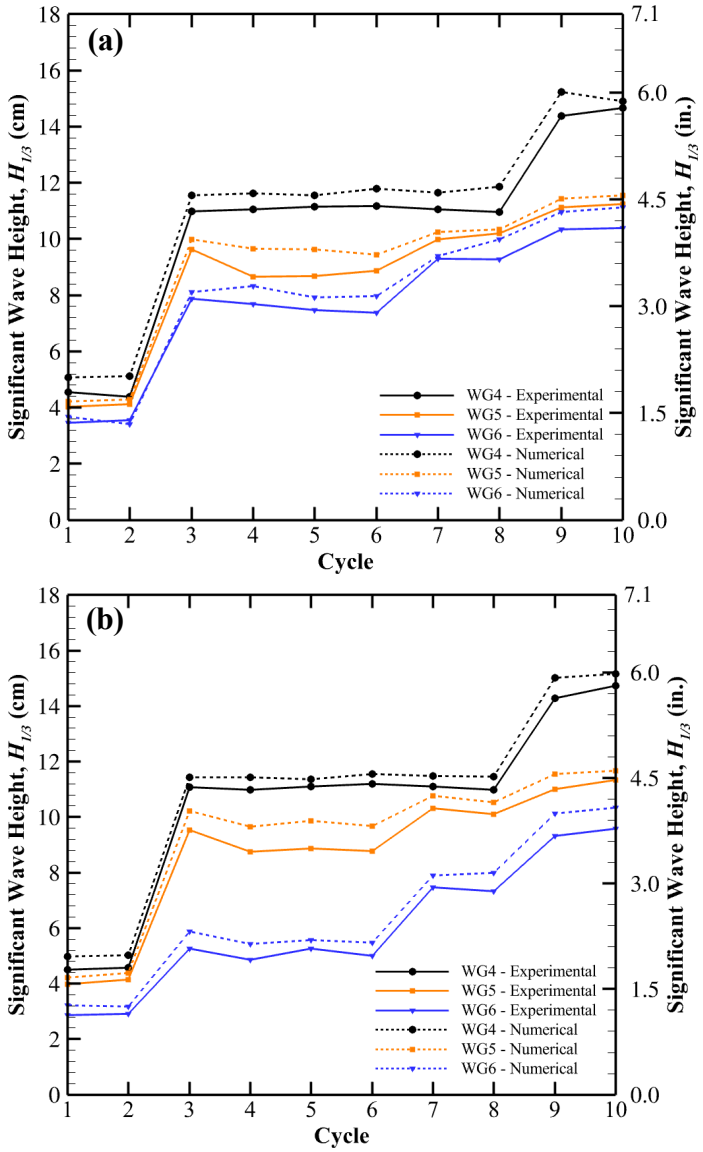

Figure 17. Transformation of significant wave height ($H_{1/3}$): (a) Unprotected configuration; (b) Mangrove protected configuration.

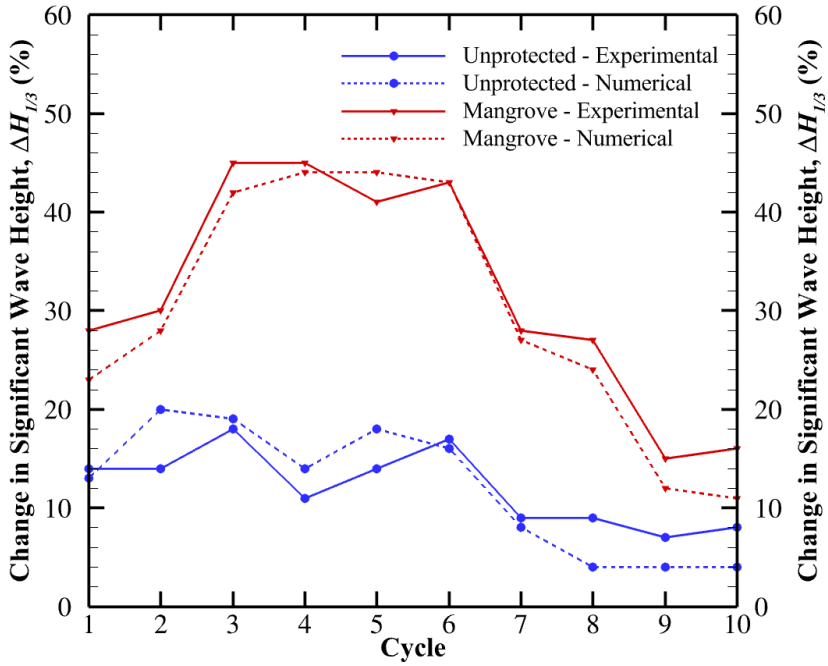

Figure 18. Change in significant wave height ($\Delta H_{1/3}$) between WG5 and WG6 for unprotected and mangrove-protected configurations.

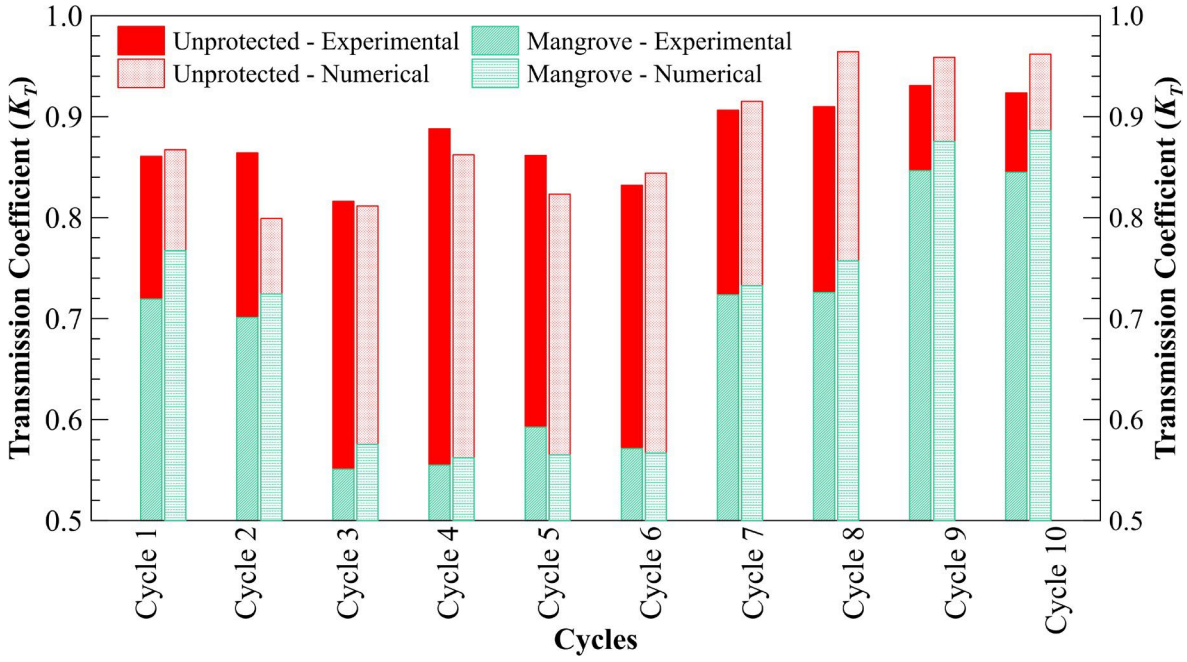

Figure 19. Variation in transmission coefficient (K_T) for unprotected and mangrove-protected configuration.

Embankment Erosion and Profile Evolution

Mechanism of Erosion

During the initial experimental phase, the upstream embankment slope underwent gradual erosional processes under low-intensity wave conditions. As successive wave cycles intensified hydrodynamic forcing, erosional rates accelerated substantially, resulting in the formation of a pronounced vertical scarp along the upstream slope face. The partially submerged condition of the embankment, with the region above still water level remaining unsaturated and maintaining structural integrity, facilitated wave impact processes that generated a distinct notch beneath the dry zone through persistent hydraulic undercutting. Subsequently, slope instability developed when the undercutting notch dimensions reached a critical geometric limit, triggering gravitational mass failure through slumping and collapse. Continued wave impingement and progressive toe erosion initiated cyclical scarp recession through alternating undercutting and slumping, a process that continued until morphological equilibrium conditions were established between erosional and depositional processes.

Furthermore, eroded sediment transport and subsequent deposition seaward of the embankment face resulted in the formation of sandbars, representing morphological adjustment to changing wave conditions. The development of the sandbars induced wave breaking away from the embankment, thereby reducing direct wave force transmission to the embankment face and providing wave energy dissipation. A pivot point was identified where net erosion and deposition processes achieved equilibrium, marking the boundary between erosional and accretional zones within the nearshore profile. While the erosional mechanisms remained consistent between unprotected and mangrove-protected configurations, morphological analysis revealed substantially greater sediment mobilization volumes in the unprotected case compared to the mangrove-protected embankment. This differential response demonstrates the effectiveness of artificial mangrove systems in mitigating wave-induced erosional processes and reducing overall sediment transport under equivalent hydrodynamic conditions.

Temporal Profile Evolution

Figure 20 presents a comparative analysis of temporal embankment profile evolution between laboratory measurements and numerical simulation results for the unprotected configuration at different time intervals: 5 min (cycle 1), 15 min (cycle 3), 30 min (cycle 6), and

60 min (cycle 10). Similarly, Figure 21 demonstrates the corresponding comparative temporal profile evolution for the mangrove-protected configuration under identical hydrodynamic conditions. The numerical simulation results reveal significant limitations in capturing the complete spectrum of erosional and sediment transport mechanisms observed in the laboratory investigation. Discrepancies can be attributed primarily to fundamental limitations within the FLOW-3D® HYDRO sediment transport model, which does not incorporate unsaturated soil parameters essential for accurately representing embankment erosion processes. The absence of unsaturated zone considerations in the sediment transport model prevents accurate simulation of capillary suction effects and moisture-dependent soil strength parameters that govern embankment stability under partial saturation conditions. As a result, the numerical model failed to capture critical failure mechanisms, including the formation of vertical scarp and the progressive undercutting processes observed in the experimental investigation. Furthermore, the numerical simulation did not successfully reproduce the prominent sandbar formation observed in the laboratory experiments. The observed numerical limitations highlight the importance of incorporating more sophisticated sediment transport formulations that account for unsaturated soil behavior and slope stability mechanisms in future modeling efforts.

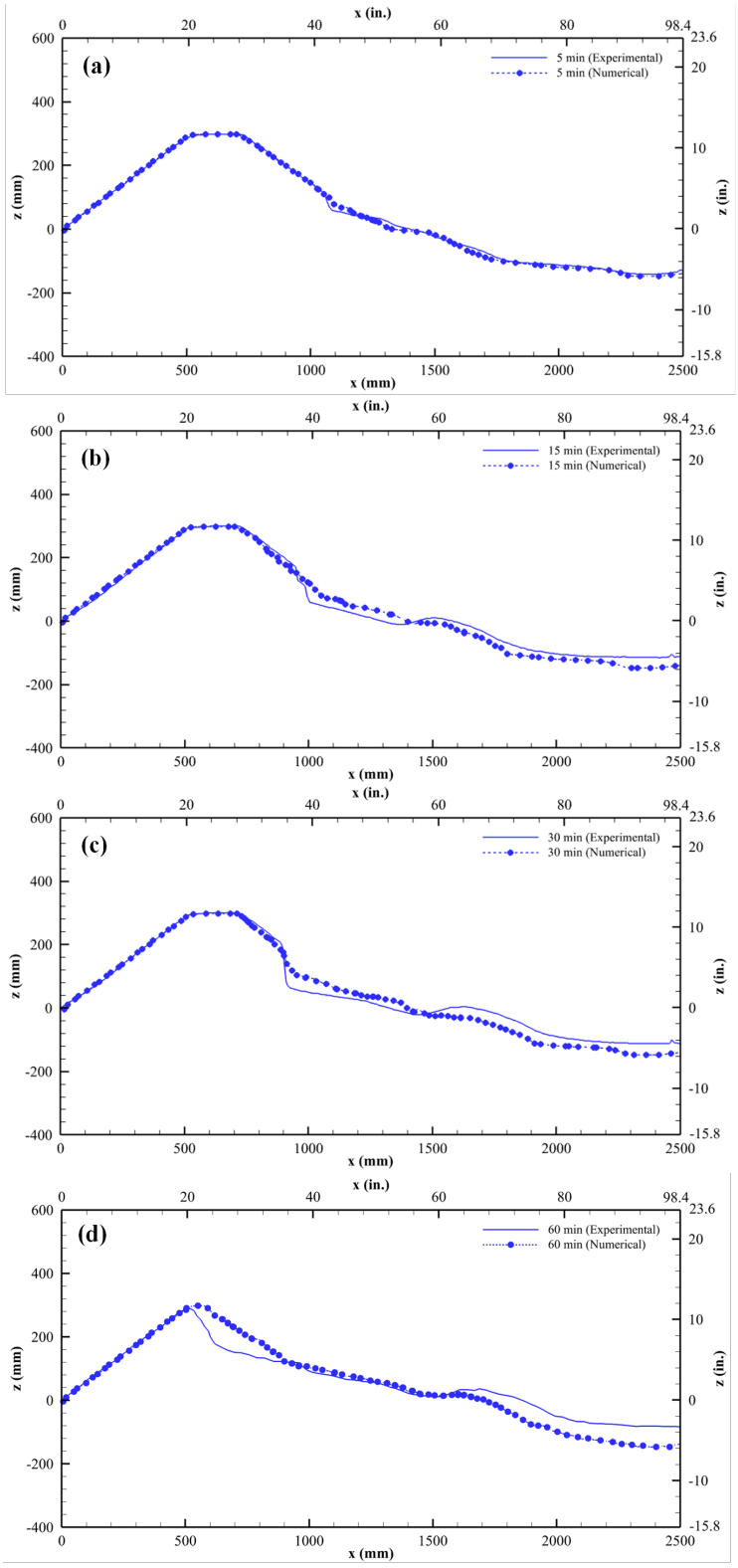

Figure 20. Comparative analysis of embankment profile evolution between laboratory experiment and numerical simulation for the unprotected configuration at temporal intervals of: (a) 5 min, (b) 15 min, (c) 30 min, (d) 60 min.

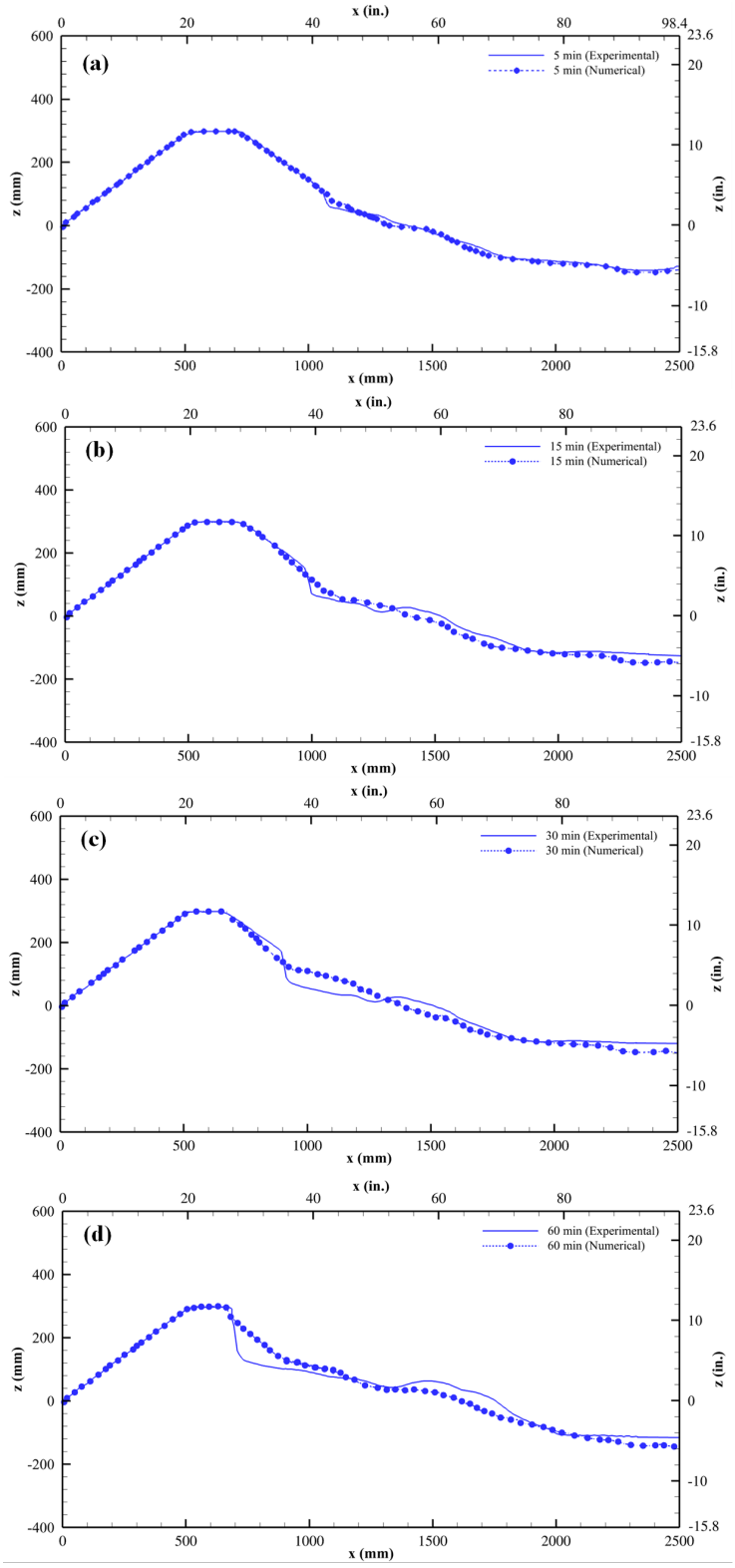

Figure 21. Comparative analysis of embankment profile evolution between laboratory experiment and numerical simulation for the mangrove protected configuration at temporal intervals of: (a) 5 min, (b) 15 min, (c) 30 min, (d) 60 min.

Figure 22 (a and b) shows the temporal evolution of embankment slope profiles derived from laboratory experimental data for both unprotected and mangrove-protected configurations, highlighting distinct morphological responses between the two cases. The spatial distribution of pivot points for the unprotected embankment showed a greater spatial distribution compared to the mangrove-protected configuration, which demonstrated more concentrated pivot point clustering. In the unprotected configuration, pivot point locations moved seaward during the initial 30 min as a result of intensifying hydraulic undercutting at the embankment toe. Subsequently, the pivot point shifted landward following slope failure and slumping, resulting in gravitational collapse that led to partial deposition of the failed material over the previously formed scarp at approximately 30 min. The artificial mangrove-protected configuration exhibited fundamentally different morphological behavior, generating comparatively smaller scarp formations during the initial 30 min relative to the unprotected embankment. Reduced erosion resulted in closely spaced pivot points. During the subsequent 30 min period, the mangrove-protected configuration showed reduced slope failure volumes compared to the unprotected case. Therefore, the deposited volume (i.e., the slump) is also comparatively smaller, which results in a smaller upslope movement of the pivot point. The location of the pivot points was a function of the scarp profile, which in turn depends on the undercutting and slump.

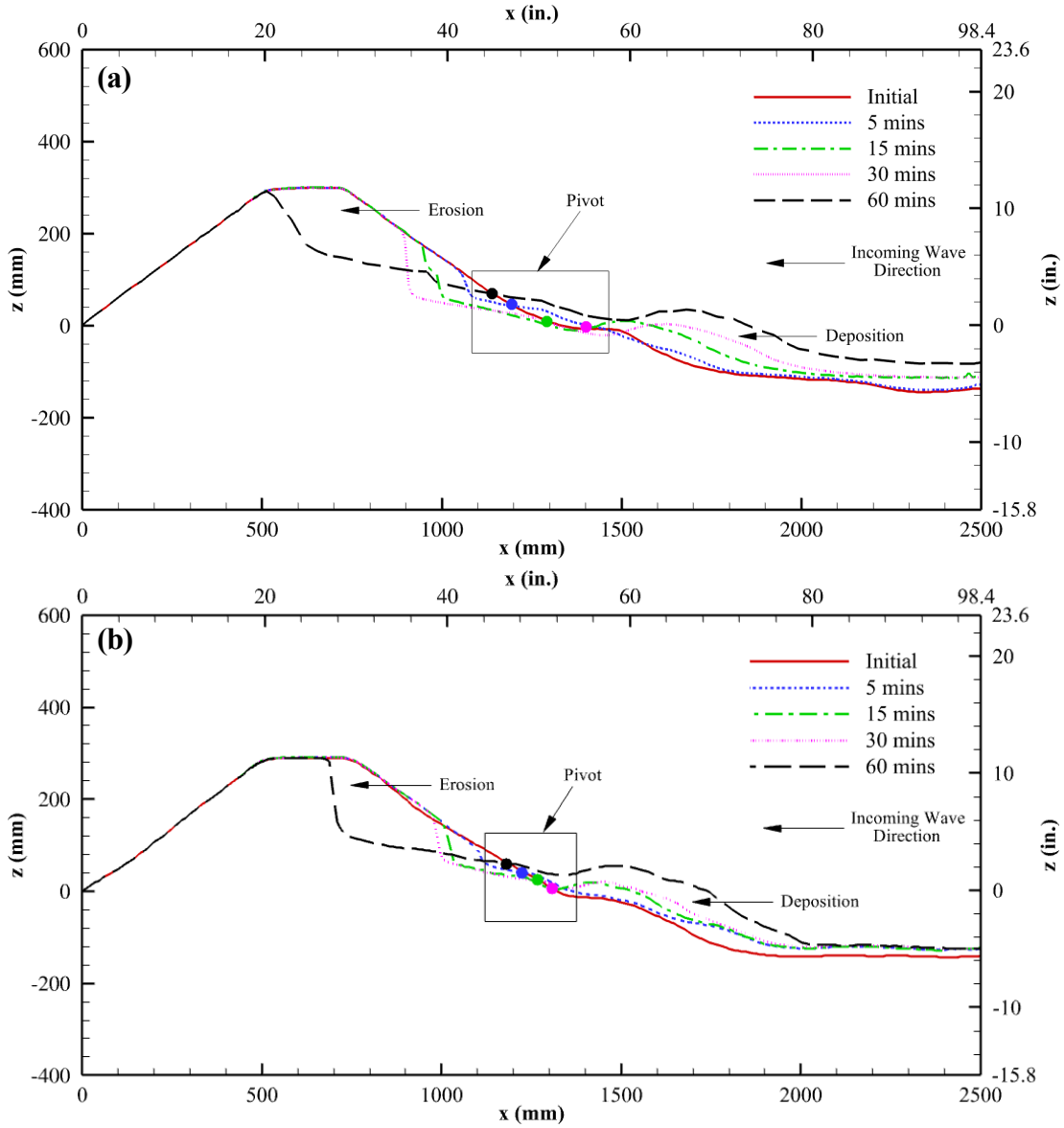

Figure 22. Temporal profile evolution of the embankment slope from laboratory study: (a) Unprotected configuration; (b) Mangrove-protected configuration.

Table 5 presents a quantitative comparison of measured erosion volumes between the unprotected configuration and the artificial mangrove-protected embankment system throughout the experimental duration. As established in the morphological analysis, the location of the pivot point, where net erosion and deposition processes achieve equilibrium, served as the reference for calculating eroded material volumes (V_E). The eroded volume was determined through geometric analysis, which involved calculating the cross-sectional area of material loss and multiplying it by

the flume width to obtain the total volumetric erosion. The experimental results demonstrate that the artificial mangrove system exhibited substantial erosion mitigation performance, with a 45% reduction in sediment mobilization during the initial 30 min testing period, when optimal hydrodynamic conditions facilitated maximum wave-mangrove interaction effectiveness. The temporal variation in protective efficiency can be attributed to the relationship between wave characteristics and the effectiveness of the mangrove root zone throughout the experimental sequence. During periods of optimal wave-vegetation interaction, when wave crests were positioned appropriately within the effective root zone elevation, maximum energy dissipation was achieved through drag and flow obstruction. Conversely, diminished protection effectiveness was observed under fully submerged conditions where elevated water levels allowed wave crests to propagate above the critical root zone, reducing the magnitude of wave-vegetation interaction and corresponding energy dissipation.

Table 5. Erosion volumes of embankment material throughout the experimental duration.

Time (mins)	**Wave Height (H) m (in.)**	**Water Depth (d) m (in.)**	**Eroded Volume (V_E) for Unprotected Section cm^3 (in.^{3})**	**Eroded Volume (V_E) for Mangrove-Protected Section cm^3 (in.^{3})**	**Percentage Decrease (%)**	**Performance of Mangrove**
5	0.05 (1.96)	0.95 (37.40)	1846 (113)	1572 (96)	15	Poor
15	0.12 (4.72)	0.95 (37.40)	7979 (487)	5708 (348)	29	Good
30	0.12 (4.72)	1.00 (39.37)	14372 (877)	7928 (484)	45	Excellent**
60	0.15 (5.92)	1.00 (39.37)	30822 (1881)	26147 (1596)	15	Poor

Note: ** – The artificial mangrove showed peak protective performance

SUMMARY AND CONCLUSIONS

This investigation evaluated the effectiveness of artificial mangrove systems in protecting coastal transportation infrastructure through a comprehensive experimental and numerical study, focusing on wave attenuation and erosion mitigation. The research addressed critical knowledge gaps in understanding how nature-inspired coastal protection systems can enhance the resilience of vulnerable highway embankments and other transportation assets exposed to coastal hazards. The experimental investigation employed a comparative approach using laboratory-scale physical modeling at Texas A&M University's Galveston Ocean Engineering Facility. Two embankment configurations were tested under identical progressive wave loading conditions: an unprotected embankment and a mangrove-protected embankment. The artificial mangrove systems were designed to replicate the morphological characteristics of *Rhizophora mangle* (red mangroves) at a 1:15 geometric scale, incorporating detailed trunk and root features, as well as staggered spatial arrangements that mimic the natural configurations of mangrove forests. The experimental program consisted of 10 sequential wave cycles with increasing wave energy, simulating the progressive intensification of a storm. Wave conditions progressed from an initial height of 0.05 m (1.96 in.) to a maximum height of 0.15 m (5.91 in.) over a total duration of 60 min. Comprehensive instrumentation included six capacitance-type wave gauges for monitoring free surface elevation and high-precision laser line scanning systems for measuring the evolution of embankment profiles. Computational validation was performed using FLOW-3D HYDRO, which incorporated physics models for gravity effects, variable density flow, turbulence modeling using the Renormalized Group (RNG) approach, and sediment transport mechanisms. The numerical framework employed multi-block meshing to optimize computational efficiency while maintaining appropriate spatial resolution in critical regions, particularly around the artificial mangrove structures.

Key Findings

1. The mangrove-protected configuration showed $H_{1/3}$ reductions ranging from 16% to 45% across all experimental cycles, compared to only 8% to 18% in the unprotected configuration.

2. Maximum energy dissipation of 44% under optimal wave-mangrove interaction conditions, with transmission coefficients (K_T) consistently lower than the unprotected configuration.
3. Optimal protection occurs during cycles when wave crests fully interact with the submerged root system. Performance diminished when elevated water levels allowed wave crests to propagate above the effective root zone.
4. The mangrove-protected configuration exhibited a 45% reduction in sediment erosion during the initial 30 min testing period, when wave-mangrove interaction was optimal.
5. Morphological analysis of embankment profile evolution revealed distinctly different responses between protected and unprotected configurations, with the mangrove-protected embankment demonstrating more concentrated pivot point clustering and sandbar formation occurring in closer proximity to the embankment structure compared to the unprotected case. The location of the pivot points is a function of the scarp profile, which in turn depends on the undercutting and slump.

Design Consideration

Maintaining appropriate relative positioning between the incoming wave and the mangrove system is essential for sustained protective effectiveness. The effective root zone elevation must be carefully designed in relation to expected water level variations to maximize the efficiency of wave-vegetation interaction. Staggered arrangements and appropriate vegetation density are crucial for optimizing energy dissipation while maintaining structural integrity.

Limitations

The experimental design employed a 1:15 geometric scaling to accommodate the dimensional constraints of the laboratory wave flume facility, representing a necessary compromise between practical feasibility and physical accuracy. While this scaling enables controlled investigation of fundamental processes, certain scale-dependent phenomena may exhibit different characteristics at full scale, particularly those involving complex three-dimensional flow interactions and long-term morphological evolution patterns. Future research would benefit from field-scale validation studies to confirm the applicability of laboratory findings to prototype conditions.

The investigation employed regular wave conditions; however, coastal environments are characterized by complex irregular wave spectra with varying directional components, wave periods, and energy distributions that may influence the effectiveness of artificial mangrove systems differently than monochromatic conditions. Investigations incorporating realistic irregular wave conditions would provide valuable insights into system performance under more representative environmental forcing.

The numerical modeling framework demonstrated capability in simulating wave propagation and hydrodynamic processes, while also highlighting opportunities for advancement in representing complex morphological phenomena. FLOW-3D® HYDRO's sediment transport formulation provides a robust computational foundation that shows potential for enhancement through the incorporation of unsaturated soil mechanics parameters, enabling more accurate representation of embankment erosion under partial saturation conditions. The numerical model has significant potential for capturing critical failure mechanisms, including vertical scarp formation and progressive undercutting processes, through future integration of geotechnical modeling components.

Concluding Remarks

This investigation provides evidence that artificial mangrove systems offer significant potential as nature-inspired solutions for protecting coastal transportation infrastructure. The experimental results demonstrate substantial wave attenuation capabilities and erosion mitigation benefits that consistently exceed the performance of unprotected embankments. The research highlights that artificial mangrove systems can achieve reductions in wave height and erosion volume under optimal conditions. These performance levels suggest that such systems could provide effective protection for vulnerable coastal highways, bridges, and other transportation assets, offering advantages over conventional hard engineering approaches, including reduced environmental impact and potentially lower life-cycle costs. However, the effectiveness of artificial mangrove systems is strongly dependent on proper design considerations, particularly the relative positioning of wave energy within the effective root zone. The temporal variation in protective performance under changing water levels highlights the importance of careful system design and potentially adaptive management strategies.

The identified limitations in current numerical modeling capabilities underscore the need for continued research into advanced computational approaches that can better represent the complex morphological processes. Future investigations should prioritize field-scale validation studies and the development of comprehensive design guidelines to facilitate the practical implementation of artificial mangrove systems.

For transportation agencies facing increasing challenges due to stress on coastal infrastructure, artificial mangrove systems represent a viable alternative that requires serious consideration in coastal resilience planning and adaptation strategies for infrastructure. The technology offers particular promise for protecting linear infrastructure assets such as coastal highways, where traditional protection measures may be prohibitively expensive or environmentally unacceptable. The successful implementation of artificial mangrove systems for protecting transportation infrastructure will require continued collaboration among transportation, coastal, and environmental engineers to optimize system performance while ensuring compatibility with broader coastal management objectives and environmental stewardship goals.

DATA AVAILABILITY STATEMENT

All data used during the study are available in the Zenodo Data Share repository with the identifier https://doi.org/10.5281/zenodo.17079709.

REFERENCES

Alongi, D. M. (2008). Mangrove forests: Resilience, protection from tsunamis, and responses to global climate change. *Estuarine, Coastal and Shelf Science*, *76*(1), 1–13. https://doi.org/10.1016/j.ecss.2007.08.024

Amos, D., & Akib, S. (2023). A Review of Coastal Protection Using Artificial and Natural Countermeasures—Mangrove Vegetation and Polymers. *Eng*, *4*(1), 941–953. https://doi.org/10.3390/eng4010055

Brinkman, R. M., Massel, S. R., Ridd, P. V., & Furukawa, K. (1997). Surface Wave Attenuation in Mangrove Forests. *Pacific Coasts and Ports'97: Proceedings of the 13th Australasian Coastal and Ocean Engineering Conference and the 6th Australasian Port and Harbour Conference*, *2*, 909–914.

Burcharth, H. F., Hawkins, S. J., Zanuttigh, B., & Lamberti, A. (2010). *Environmental design guidelines for low crested coastal structures*. Elsevier.

Chang, C., Mori, N., Tsuruta, N., Suzuki, K., & Yanagisawa, H. (2022a). An Experimental Study of Mangrove-Induced Resistance on Water Waves Considering the Impacts of Typical *Rhizophora* Roots. *Journal of Geophysical Research: Oceans*, *127*(6), e2022JC018653. https://doi.org/10.1029/2022JC018653

Chang, C., Mori, N., Tsuruta, N., Suzuki, K., & Yanagisawa, H. (2022b). An Experimental Study of Mangrove-Induced Resistance on Water Waves Considering the Impacts of Typical *Rhizophora* Roots. *Journal of Geophysical Research: Oceans*, *127*(6), e2022JC018653. https://doi.org/10.1029/2022JC018653

Chen, Z., Ortiz, A., Zong, L., & Nepf, H. (2012). The wake structure behind a porous obstruction and its implications for deposition near a finite patch of emergent vegetation. *Water Resources Research*, *48*(9), 2012WR012224. https://doi.org/10.1029/2012WR012224

Coastal Engineering Research Center (US). (1973). *Shore protection manual* (Vol. 1). US Army Coastal Engineering Research Center.

Dawson, D. A., Hunt, A., Shaw, J., & Gehrels, W. R. (2018). The Economic Value of Climate Information in Adaptation Decisions: Learning in the Sea-level Rise and Coastal Infrastructure Context. *Ecological Economics*, *150*, 1–10. https://doi.org/10.1016/j.ecolecon.2018.03.027

Dean, R. G., & Dalrymple, R. A. (1991). *Water wave mechanics for engineers and scientists* (Vol. 2). World Scientific.

Douglass, S. L., Webb, B. M., & Kilgore, R. (2014). *Highways in the Coastal Environment: Assessing Extreme Events* (No. FHWA-NHI-14-006). Federal Highway Administration.

Fatimah, E., Wahab, A. K. A., & Ismail, H. (2008). *Numerical modeling approach of an artificial mangrove root system (ArMS) submerged breakwater as wetland habitat protector*.

Figlus, J., Sigren, J. M., Armitage, A. R., & Tyler, R. C. (2014). Erosion of vegetated coastal dunes. *Coastal Engineering Proceedings*, *1*, 20. https://doi.org/10.9753/icce.v34.sediment.20

Furukawa, K., Wolanski, E., & Mueller, H. (1997). Currents and Sediment Transport in Mangrove Forests. *Estuarine, Coastal and Shelf Science*, *44*(3), 301–310. https://doi.org/10.1006/ecss.1996.0120

Hirt, C. W., & Nichols, B. D. (1981). Volume of fluid (VOF) method for the dynamics of free boundaries. *Journal of Computational Physics*, *39*(1), 201–225. https://doi.org/10.1016/0021-9991(81)90145-5

Hoque, A., Husrin, S., & Oumeraci, H. (2018). Laboratory studies of wave attenuation by coastal forest under storm surge. *Coastal Engineering Journal*, *60*(2), 225–238. https://doi.org/10.1080/21664250.2018.1486268

Hughes, S. A. (1993). *Physical models and laboratory techniques in coastal engineering* (Vol. 7). World Scientific.

Ismail, H., Abd Wahab, A. K., & Alias, N. E. (2012). Determination of mangrove forest performance in reducing tsunami run-up using physical models. *Natural Hazards*, *63*(2), 939–963. https://doi.org/10.1007/s11069-012-0200-y

Kazemi, A., Van De Riet, K., & Curet, O. M. (2017). Hydrodynamics of mangrove-type root models: The effect of porosity, spacing ratio and flexibility. *Bioinspiration & Biomimetics*, *12*(5), 056003. https://doi.org/10.1088/1748-3190/aa7ccf

Li, X., Van Paassen, L., & Tao, J. (2022). Investigation of using mangrove-inspired skirt pile group as a scour countermeasure. *Ocean Engineering*, *266*, 113133. https://doi.org/10.1016/j.oceaneng.2022.113133

Libby, M., Tomiczek, T., Cox, D., & Lomónaco, P. (2024). The sum of the parts: Green, gray, and green-gray infrastructure to mitigate wave overtopping. *Coastal Engineering*, *194*, 104615. https://doi.org/10.1016/j.coastaleng.2024.104615

Linham, M. M., & Nicholls, R. J. (2010). *Technologies for Climate Change Adaptation—Coastal Erosion and Flooding*. University of Sothampton.

Maza, M., Adler, K., Ramos, D., Garcia, A. M., & Nepf, H. (2017). Velocity and Drag Evolution From the Leading Edge of a Model Mangrove Forest. *Journal of Geophysical Research: Oceans*, *122*(11), 9144–9159. https://doi.org/10.1002/2017JC012945

Maza, M., Lara, J. L., & Losada, I. J. (2015). Tsunami wave interaction with mangrove forests: A 3-D numerical approach. *Coastal Engineering*, *98*, 33–54. https://doi.org/10.1016/j.coastaleng.2015.01.002

Maza, M., Lara, J. L., & Losada, I. J. (2019). Experimental analysis of wave attenuation and drag forces in a realistic fringe Rhizophora mangrove forest. *Advances in Water Resources*, *131*, 103376. https://doi.org/10.1016/j.advwatres.2019.07.006

Maza, M., Lara, J. L., & Losada, I. J. (2021). Predicting the evolution of coastal protection service with mangrove forest age. *Coastal Engineering*, *168*, 103922. https://doi.org/10.1016/j.coastaleng.2021.103922

Mazda, Y., Magi, M., Ikeda, Y., Kurokawa, T., & Asano, T. (2006). Wave reduction in a mangrove forest dominated by Sonneratia sp. *Wetlands Ecology and Management*, *14*(4), 365–378. https://doi.org/10.1007/s11273-005-5388-0

Mazda, Y., Magi, M., Kogo, M., & Hong, P. N. (1997). Mangroves as a coastal protection from waves in the Tong King delta, Vietnam. *Mangroves and Salt Marshes*, *1*(2), 127–135. https://doi.org/10.1023/a:1009928003700

Mcmann, D., Keck, J., Tomiczek, T., Lomonaco, P., Cox, D., & Libby, M. (2024). Small-Scale Experiments' Ability To Augment Large Lab Testing For Designing Nature-Based And Hybrid Solutions For Coastal Flood Hazard Mitigation. *CoastLab 2024: Physical Modelling in Coastal Engineering and Science*. https://doi.org/10.59490/coastlab.2024.697

Morris, R. L., Konlechner, T. M., Ghisalberti, M., & Swearer, S. E. (2018). From grey to green: Efficacy of eco-engineering solutions for nature-based coastal defence. *Global Change Biology*, *24*(5), 1827–1842. https://doi.org/10.1111/gcb.14063

Nicolle, A., & Eames, I. (2011). Numerical study of flow through and around a circular array of cylinders. *Journal of Fluid Mechanics*, *679*, 1–31. https://doi.org/10.1017/jfm.2011.77

Ohira, W., Honda, K., Nagai, M., & Ratanasuwan, A. (2013). Mangrove stilt root morphology modeling for estimating hydraulic drag in tsunami inundation simulation. *Trees*, *27*(1), 141–148. https://doi.org/10.1007/s00468-012-0782-8

Ozeren, Y., Wren, D. G., & Reba, M. L. (2021). Wave-Induced Erosion of Soil Embankment in Laboratory Flume. *Journal of Hydraulic Engineering*, *147*(4), 04021011. https://doi.org/10.1061/(ASCE)HY.1943-7900.0001866

Quang Bao, T. (2011). Effect of mangrove forest structures on wave attenuation in coastal Vietnam. *Oceanologia*, *53*(3), 807–818. https://doi.org/10.5697/oc.53-3.807

Quartel, S., Kroon, A., Augustinus, P. G. E. F., Van Santen, P., & Tri, N. H. (2007). Wave attenuation in coastal mangroves in the Red River Delta, Vietnam. *Journal of Asian Earth Sciences*, *29*(4), 576–584. https://doi.org/10.1016/j.jseaes.2006.05.008

Soulsby, R. (1997). *Dynamics of marine sands*.

Strusińska-Correia, A., Husrin, S., & Oumeraci, H. (2013). Tsunami damping by mangrove forest: A laboratory study using parameterized trees. *Natural Hazards and Earth System Sciences*, *13*(2), 483–503. https://doi.org/10.5194/nhess-13-483-2013

Sutton-Grier, A. E., Wowk, K., & Bamford, H. (2015). Future of our coasts: The potential for natural and hybrid infrastructure to enhance the resilience of our coastal communities, economies and ecosystems. *Environmental Science & Policy*, *51*, 137–148. https://doi.org/10.1016/j.envsci.2015.04.006

Sweet, W. V., Kopp, R. E., Weaver, C. P., Obeysekera, J., Horton, R. M., Thieler, E. R., & Zervas, C. (2017). *Global and Regional Sea Level Rise Scenarios for the United States* [CO-OPS 083].

Tomiczek, T., Wargula, A., Lomónaco, P., Goodwin, S., Cox, D., Kennedy, A., & Lynett, P. (2020). Physical model investigation of mid-scale mangrove effects on flow hydrodynamics and pressures and loads in the built environment. *Coastal Engineering*, *162*, 103791. https://doi.org/10.1016/j.coastaleng.2020.103791

Van Rijn, L. C. (1984). Sediment Transport, Part I: Bed Load Transport. *Journal of Hydraulic Engineering*, *110*(10), 1431–1456. https://doi.org/10.1061/(ASCE)0733-9429(1984)110:10(1431)

Vo-Luong, P., & Massel, S. (2008). Energy dissipation in non-uniform mangrove forests of arbitrary depth. *Journal of Marine Systems*, *74*(1–2), 603–622. https://doi.org/10.1016/j.jmarsys.2008.05.004

Yin, Z., Li, J., Wang, Y., Wang, H., & Yin, T. (2023). Solitary wave attenuation characteristics of mangroves and multi-parameter prediction model. *Ocean Engineering*, *285*, 115372. https://doi.org/10.1016/j.oceaneng.2023.115372

Zhang, K., Liu, H., Li, Y., Xu, H., Shen, J., Rhome, J., & Smith, T. J. (2012). The role of mangroves in attenuating storm surges. *Estuarine, Coastal and Shelf Science*, *102–103*, 11–23. https://doi.org/10.1016/j.ecss.2012.02.021

Zhang, X., Chua, V. P., & Cheong, H.-F. (2015). Hydrodynamics in mangrove prop roots and their physical properties. *Journal of Hydro-Environment Research*, *9*(2), 281–294. https://doi.org/10.1016/j.jher.2014.07.010

Zong, L., & Nepf, H. (2012). Vortex development behind a finite porous obstruction in a channel. *Journal of Fluid Mechanics*, *691*, 368–391. https://doi.org/10.1017/jfm.2011.479